AFRL-RX-WP-TR-2016-0102

TECHNICAL OPERATIONS (TOPS) IV
Task Order 0003: Responsive Interface for Transport Tuning (RITT)

Keith Slinker and Corey Kondash

Universal Technology Corporation

29 MAY 2016
FINAL REPORT

(STINFO COPY)

AIR FORCE RESEARCH LABORATORY
MATERIALS AND MANUFACTURING DIRECTORATE
WRIGHT-PATTERSON AIR FORCE BASE, OH 45433-7750
AIR FORCE MATERIEL COMMAND
UNITED STATES AIR FORCE

NOTICE AND SIGNATURE PAGE

_____//SIGNATURE//_____   ____//SIGNATURE//_____
JEFFERY BAUR   MICHAEL J. KINSELLA
Project Engineer   Chief
Composites Materials & Processing Section   Composites Branch
Structural Materials Division   Structural Materials Division
Materials & Manufacturing Directorate   Materials & Manufacturing Directorate

_____//SIGNATURE//_____
ROBERT T. MARSHALL
Chief
Structural Materials Division
Materials & Manufacturing Directorate

REPORT DOCUMENTATION PAGE

Form Approved
OMB No. 0704-0188

1. REPORT DATE *(DD-MM-YYYY)*	2. REPORT TYPE	3. DATES COVERED *(From – To)*
29 May 2016	Final Report	29 October 2012 – 29 April 2016

4. TITLE AND SUBTITLE	5a. CONTRACT NUMBER
TECHNICAL OPERATIONS (TOPS) IV	FA8650-11-D-5800-0003
Task Order 0003: Responsive Interface for Transport Tuning (RITT)	**5b. GRANT NUMBER**
	5c. PROGRAM ELEMENT NUMBER 62102F

6. AUTHOR(S)	5d. PROJECT NUMBER
Keith Slinker and Corey Kondash	4347
	5e. TASK NUMBER
	5f. WORK UNIT NUMBER X0HA

7. PERFORMING ORGANIZATION NAME(S) AND ADDRESS(ES)	8. PERFORMING ORGANIZATION REPORT NUMBER
Universal Technology Corporation 1270 N. Fairfield Road Dayton, OH 45432-2600	

9. SPONSORING / MONITORING AGENCY NAME(S) AND ADDRESS(ES)	10. SPONSOR/MONITOR'S ACRONYM(S)
Air Force Research Laboratory Materials and Manufacturing Directorate Wright-Patterson Air Force Base, OH 45433-7750 Air Force Materiel Command United States Air Force	AFRL/RXCC
	11. SPONSOR/MONITOR'S REPORT NUMBER(S) AFRL-RX-WP-TR-2016-0102

12. DISTRIBUTION / AVAILABILITY STATEMENT

Distribution Statement A. Approved for public release; distribution unlimited.

13. SUPPLEMENTARY NOTES

PA Case Number: 88ABW-2016-5465; Clearance Date: 28 October 2016. This document contains

14. ABSTRACT (Maximum 200 words)

This report summarizes research activity performed under this task order. The overall objective was to develop novel material interfaces with the potential to respond to changes in mechanical, thermal, or electromagnetic stimulus. The primary thrust was on the further development of artificial hair sensors (AHS) featuring a responsive carbon nanotube (CNT) array to serve as a piezoresistive element. This report outlines the fabrication and modeling of these systems, along with investigation of their potential for several applications of AFRL interest. Additionally, the task order included a preliminary investigation of polymer matrix composites under laser irradiation, which is reported under separate cover, as AFRL Interim Report AFRL-RX-WP-TR-2016-0071 dated 30 October 2015.

15. SUBJECT TERMS

artificial hair sensor, carbon nanotube, piezoresistive element, organic matrix composites, layered polymeric materials, nanotube microfiber, aligned CNT film

16. SECURITY CLASSIFICATION OF:			17. LIMITATION OF ABSTRACT	18. NUMBER OF PAGES	19a. NAME OF RESPONSIBLE PERSON *(monitor)*
			SAR	70	Jeffery Baur
a. REPORT Unclassified	**b. ABSTRACT** Unclassified	**c. THIS PAGE** Unclassified			**19b. TELEPHONE NUBER** *(include area code)* (937) 255-9649

Standard Form 298 (Rev. 2-89)
Prescribed by ANSI Std. Z39-18

Table of Contents

List of Figures

List of Tables

1.0 SUMMARY

This report summarizes activity accomplished under Technical Operations IV (TOPS IV), Task Order 0003. Through this effort, Universal Technology Corporation (UTC) provided onsite and extramural technical support for the Organic Matrix Composites (OMC) Materials and Processes (M&P) Research Team of the Air Force Research Laboratory, Materials and Manufacturing Directorate, Structural Materials Division, Composites Branch (AFRL/RXCC) from 29 October 2012 to 29 April 2016.

The objective of this effort was to develop novel material interfaces with the potential to respond to changes in mechanical, thermal, or electromagnetic stimulus. The thrust of this effort was on the further development of artificial hair sensors (AHS) featuring a responsive carbon nanotube (CNT) array to serve as a piezoresistive element. This report outlines the fabrication and modeling of these systems, along with their study towards several applications of AFRL interest.

In addition to the AHS research and development (R&D), work under this task order supported a combined team investigating the interaction of polymer matrix composites under high energy laser irradiation. UTC provided both experimental and modeling support for this work, as reported in a separate technical report, AFRL-RX-WP-TR-2016-0071 dated 30 October 2015. Within the scope of this task order, UTC also provided financial assistance to the Massachusetts Institute of Technology (MIT) for preliminary investigation of aligned CNT films as resistive heaters for out-of-oven curing of polymer composites, summarized in Appendix B.

2.0 INTRODUCTION

Detection of air flow by hair sensors is inspired by the ability of many animals to detect changes in their environment with distributed arrays of flow-sensitive hairs. [1-4] For example, the locust performs angle of sideslip (AoS) regulation from hair sensor airflow feedback of flow patterns that evolve over its head. [3] Independent of biological inspiration, engineered angle of attack (AoA) and AoS measurement technologies known as air data systems (ADS) were developed relying on pressure sensor arrays located at the nose of various high speed air and spacecraft. [5] In contrast to pressure sensors, AHS are a more information rich source of data because their response is determined from a flow velocity field with both magnitude and direction [6], as opposed to a scalar pressure field with pressure sensor-based ADS. Additionally, micro-scale AHS are suitable flow sensor candidates for insect-to-bird scale, low-Reynolds-number flyers, due to their low power consumption, light weight, high sensitivity, and small footprint. AHS are plausible technologies for aeronautic applications, such as attitude control, heading determination, and self-stabilization. [7,8] These qualities are also attractive for mechanical sensors that can be embedded in structural materials, such as composites. A need exists for sensors that are capable of rapidly transducing small changes in deflection into detectable signals. Many such sensors could be easily distributed over aircraft surfaces for detection of spatial airflow or mechanical deformation. Ideally, sensors for either application would exhibit high sensitivity and possess mechanics robust enough to be embedded in a wing or composite structure.

CNTs can be synthesized into self-aligned arrays that can exhibit large piezoresistance in response to compression [9-11], and the synthesis of CNT arrays and their subsequent mechanical, electrical, and thermal properties have been widely studied. [12-18] Synthesis of nanotube arrays on structural microfibers, in this case aligned radially from the fiber surface, has been investigated. [19-21] Composites of these "fuzzy fibers" can exhibit improved electrical and thermal conductivity [22] and enhanced structural properties, such as toughness [23,24] and interlaminar shear. [25-27] While significant work has been performed on planar arrays and the growth on reinforcement fibers, research into the synthesis of CNT arrays within confined geometries is limited. Envisioned applications require the growth or placement of the nanotube array within a pore, between closely spaced planar surfaces, or within a tow or weave of composite fibers. However, the high aspect ratio of such geometries could represent a challenge in that the catalyst, carbon source, and synthesis conditions must all be present for robust growth of the self-aligned CNT arrays.

The electromechanical properties of CNT arrays have been initially investigated and evaluated for use in various applications. CNT arrays on glass fibers have been demonstrated as embedded strain sensors in composites when expanded along the fiber. [28,29] CNT arrays on planar substrates, when compressed against a metalized surface, have been shown to demonstrate a large decrease in resistance, which can be attributed to changes both in the CNT-metal contact resistance and the bulk CNT array piezoresistivity. [9-11] The mechanical properties of planar CNT arrays have been directly characterized [11,13-15,30-33], but these properties have not been as widely reported for CNT arrays on fibers. In either case The ability to correlate the piezoresistivity and related compressive modulus of CNT arrays to growth conditions, or any alternative to direct measurement of these properties, has yet to be demonstrated.

The fabrication, characterization, and modeling of a relatively new class of embedded AHS is discussed in this report. Structural glass microfibers with high specific stiffness serve as the hair element. The piezoresistive nanotube array on the fibers transduce the deflection of the hair into changes in resistance when compressed inside the metal coated glass capillary. [21,34,35] A model for the growth of the nanotubes within such high aspect ratio microcavities is demonstrated, and it is based on diffusion of the reactants and intermediates within the pore of the capillary and first order reaction kinetics on the surface of the fiber. The response to quasi-static deflections from a point load in a laboratory-scale setup is correlated to the distributed load response experienced within an air flow. These point load deflections are fitted to a model treating the nanotube support as an elastic base, and the stiffness of the radial nanotube array is derived. The resonant frequencies of the sensor are found by perturbing a sensor at acoustic frequencies to probe the dynamic response of the sensors. It is shown that these frequencies agree with those predicted for an elastic base if the stiffness from the quasi-static measurements is used. Finally, a new application for these deflection-based sensors is introduced. A mechanical shear sensor is created when one of these sensors is imbedded in a bonded composite. The resulting sensor is capable of measuring the displacement between adherends in a lap shear test.

3.0 METHODS, ASSUMPTIONS, AND PROCEDURES

3.1 CNT-Based Hair Sensors: Fabrication and Model Parameterization

3.1.1 Introduction

MEMS-based, bottom-up processes are well established for fabricating precision microscale devices over a small coverage area at relatively high capital cost. However, the devices described here result from the direct assembly of microscale constituents and batch processing to rapidly fabricate large numbers of sensors that can then be individually positioned at any desired spacing. Besides being of the desired scale, the Young's modulus (E) of the structural glass microfiber hairs in these devices (86.9 GPa (12,604 ksi), according to the manufacturer) is much larger than that of the polymer hairs fabricated in MEMS devices and is a major contributor to their comparatively higher sensitivity and bandwidth. It is shown in the following sections that the response of the sensor is a function of the properties of the constituents, so predicting or calibrating the response of the hair depends on determining the properties to parameterize supporting models. In particular, the stiffness of the self-assembled nanotube array varies in a way that cannot yet be predicted, so a method for measuring the stiffness in the sensors is presented and demonstrated. In general, processes for fabricating, screening, tuning, and parameterizing hair sensors with structural microfiber hairs supported by CNT arrays are described.

3.1.2 Sensor Fabrication

The hairs are glass microfibers (AGY 933 S-2) with a radius (r) of 4.5 µm, a density (ρ) of 2,580 kg/m^3 (161.1 lb/ft^3), and a bending stiffness (EI) of 28 Nµm^2 (67.8 lbf-ft^2). The fibers are uniformly coated with a layer of alumina approximately 10 nm thick by atomic layer deposition (Cambridge NanoTech). The pore for the hair is a glass microcapillary (Polymicro Technologies - Molex) with off-the-shelf inner radius (R) of 12.5 µm (0.492 mil), and cut and polished in batch to a final length of 1.2 mm (47 mil). Numerous capillaries are mounted on end in a holder, and gold electrodes are deposited by sputtering at an angle such that the gold coats the inside walls of the capillaries to a depth approximately equal to twice the diameter. The process is repeated for the other end of the capillaries, with the metal continuing onto the faces and sides on both ends. The holder acts as a physical mask, blocking the deposition in the middle to electrically isolate the two ends. The glass fibers are cut to length and inserted into the microcapillaries.

The entire assemblies are subjected to CNT synthesis (Section 3.2) in a tube furnace at 750 °C (1,382 °F) by continuous liquid injection of a ferrocene/xylene mixture that vaporizes near the opening of the furnace and is transported to the sample with argon and hydrogen gases. [21,34,35] The CNTs grow preferentially on the alumina-coated glass fiber and radially from the fiber surface as a low density array of wavy, vertically-aligned, entangled CNTs. The height of the array ($L_{CNT}(x)$) is approximately equal to the length of the CNTs and can vary with axial position (x) both inside and outside the capillary. As will be discussed later, the sensitivity generally decreases with nanotube length since the nanotube array acts as a strain sensor. Secondly, rather than uniformly decreasing the local density of the array as the total diameter increases with increasing CNT length, the nanotubes in the array will eventually separate in sections from neighboring CNTs. These bifurcations occurs at CNT lengths much greater than 10 microns during growth on these curved, small-radius fiber surfaces and have the appearance

of inverted mohawk hair styles. The small microcapillary radius was chosen to maintain radial uniformity and maximize the sensitivity of the sensors.

As it grows, the CNT array self-positions the glass fiber near the radial center of the capillary. The growth conditions, particularly the duration of growth, determine the length of the CNTs and therefore the total diameter of the nanotube coated fiber ($D(x) = 2r + 2L_{CNT}(x)$). While $D(x)$ is typically less than or equal to the inner diameter of the capillary ($2R$), functioning sensors can also be fabricated if the CNTs are allowed to continue growing to longer lengths. In this case, the diameter outside the capillary is increased while the internal diameter matches the diameter of the capillary; however, the curvature of the nanotubes and density of the array inside the capillary both appear larger. After CNT synthesis, the hair is fixed to the bottom capillary face with epoxy to prevent axial movement.

A cross-sectional schematic of these hair-in-pore sensors is shown in Figure 1 (left). A scanning electron microscope (SEM) image of a device is shown in Figure 1 (right) for which the nanotubes external to the capillary have been removed by focused ion beam (FIB) for imaging purposes. In the device pictured, the nanotubes completely fill up the space between the capillary and the pore at the opening. However, $D(x)$ at the opening of the capillary is less than $2R$ for many of the devices discussed here. In all cases, and despite $D(x)$ being less than $2R$ for some devices, the nanotube array mechanically supports the glass fiber down the length of the capillary and forms an electrical path between the two electrodes.
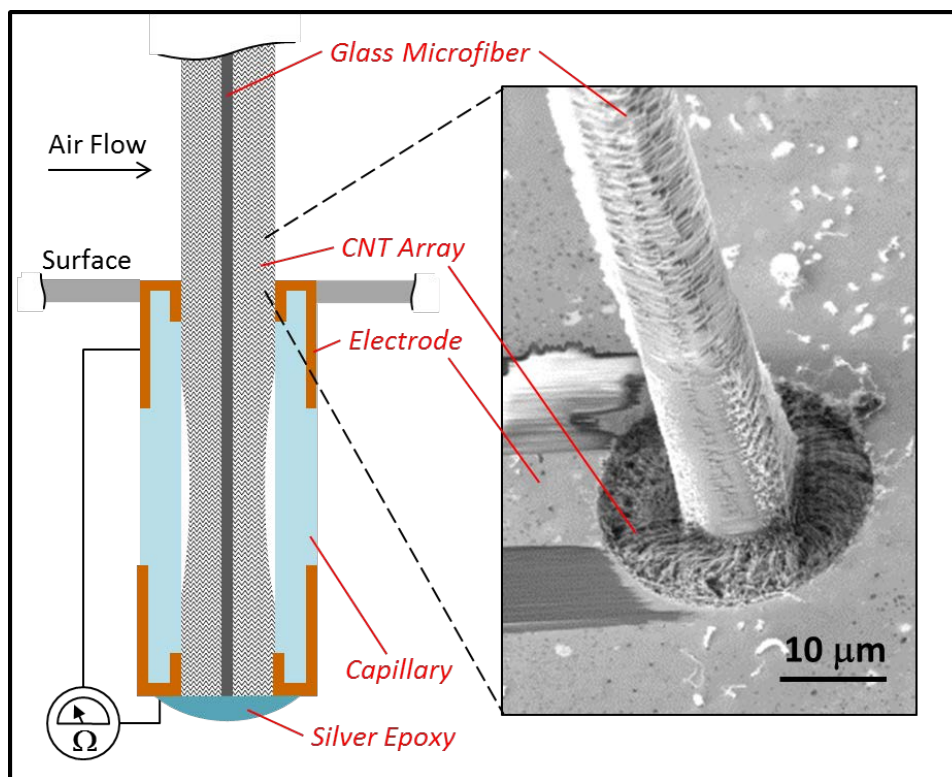
Figure 1. Schematic (Left) and SEM Image (Right) of Nanotube-Microfiber AHS

Note: (Left) Cross-sectional schematic of nanotube-microfiber AHS (not to scale). The alumina-coated glass microfiber hair is inserted into the glass capillary pore (with pre-deposited top and bottom electrodes) prior to CNT synthesis. The CNT array grows radially from the microfiber along its entire length, self-positioning the fiber at the center of the pore. After synthesis, the fiber is affixed at the base

of the capillary with silver epoxy. (Right) SEM image looking down at the top of the capillary opening. A focused ion beam was used to remove the CNTs from the fiber to expose the CNT array just inside the pore for imaging.

3.1.3   Tuning and Baseline Response

When the fiber is deflected by external forces, the CNT array at the opening is compressed against the capillary electrode, thereby transducing the deflection of the hair into a (typically) decrease in resistance. While this resistance decrease is due in part to the increase in nanotube-to-nanotube connections in the bulk of the array, it has been shown in compression measurements of planar arrays that this response is dominated by the changing CNT-metal contact resistance. [9] The electrode is continuous around the perimeter of the capillary, so the response of the sensor is typically independent of the direction of the applied force (omnidirectional response). A directional response could be obtained by sectioning the electrode, but this would increase the complexity of the manufacturing process. Also, while resistance typically decreases with hair deflection (as the nanotubes are compressed against the side of the capillary opposite the applied force), the symmetric nature of the device produces a corresponding increase in resistance (as the nanotubes are relaxed from the capillary) on the side of the applied force (see Figure 2). While a resistance increase is occasionally observed for very small deflections of the hair in some devices, a decrease in resistance is observed in all devices as the hair is continued to be deflected since the CNT compression dominates these parallel conduction paths.
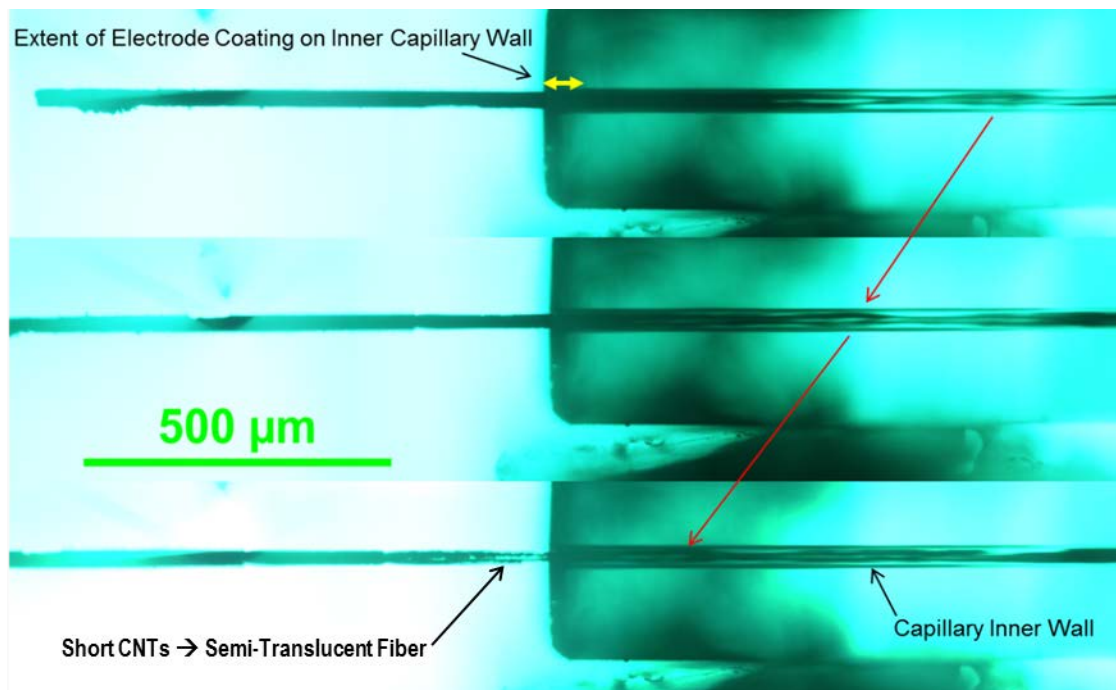
Figure 2. Optical Image of a Hair Sensor

Note: A back-lit optical image of a hair sensor looking at the exposed hair on the left and at the internal portion of the hair through the capillary on the right. The height of the nanotube array (or total CNT-glass diameter) is largely uniform along the length of the exposed hair. Inside the capillary, the nanotube array is of similar height at the opening of the capillary, but has reduced height toward the midpoint of

the capillary. The CNTs are short enough in some places that the light can shine through the fiber, making it appear translucent even though it is coated with black CNTs throughout. The top image shows the sensor as fabricated, followed by images of the sensor after the hair has been shifted out of the capillary by 225 and 275 μm (8.86 and 10.8 mil), respectively (tracked by the arrows).

Long capillary lengths are more easily manipulated and allow the hair to be completely mechanically supported by the CNTs. Conversely, the nanotubes tend to be shorter towards the axial middle of the capillary due to the competition between CNT growth and the diffusion of the gaseous carbon components from the open ends (Section 3.2). An optical image of a sensor is shown in Figure 2. The image is back lit through the transparent capillary such that the nanotube coated hair is visible both outside and inside the capillary. The nanotube array is highly optically absorbing and appears black in the image; however, in areas where the nanotubes are short or absent, the nanotube-coated glass fiber is transparent. The nanotube height is fairly constant outside the capillary with a total nanotube-glass-fiber diameter of about 25 μm (0.98 mil). Inside the capillary, the nanotube array is of similar height near the opening, but the nanotubes are shorter toward the axial middle of the capillary.

As discussed in Section 3.3 and briefly below, the sensitivity of the sensors is determined in part by the length of the nanotubes near the opening, which is the electrode-coated region of the capillary. The top image of Figure 2 shows the sensor as fabricated, followed by two images of the sensor after the hair was shifted out of the capillary in two increments. In each case, the hair was then deflected by 100 μm (3.94 mil) by a point load applied 530 μm (20.9 mil) from the capillary opening, and the change in resistance was measured. In the as-grown sensor in Figure 2, the nanotubes fill up the capillary opening, and the decrease in resistance was less than 0.5%. In the second image, the nanotube-fiber diameter is at or slightly less than the inner diameter of the capillary, resulting in a significant 7% decrease in resistance as the fiber was deflected. In the third image, the shortest nanotube array throughout the length of the fiber is within the metallized portion of the capillary. No resistance change was observed at this magnitude of deflection, possibly because the deflection of the base of the fiber was not large enough to bring the nanotube array into contact with the capillary wall. In Section 3.3, it is shown that working devices can be realized even with such short nanotubes. Also, the sensitivity can be changed by over 2 orders of magnitude, in-part by adjusting the length of the nanotubes at the opening. Assuming electrical continuity, the hairs can be axially repositioned after growth to bring shorter nanotubes into the transducing region, thereby tuning the response of sensors even after CNT-synthesis.

A benchtop test fixture for quasi-static screening, tuning, and parameterizing the hair sensors is shown in Figure 3. Non-permanent, four-point electrodes are pressed against the sensor to prevent damage to the sensor and allow for imaging of the capillary body and hair. The capillary can be backlit through the semi-transparent 3D-printed fixture. A point load is applied with a razor blade, and the distance from the base of the hair that the load is applied (L_P) can be adjusted by altering the relative position of the two parts of the fixture. The magnitude of the deflection is changed incrementally or continuously by the position of a microactuator. A voltage is applied to the device with a Keithley 2400 SourceMeter, and the resulting resistance is also measured with the Keithley 2400. The position of the microactuator and device resistance are correlated and automatically recorded with a computer.
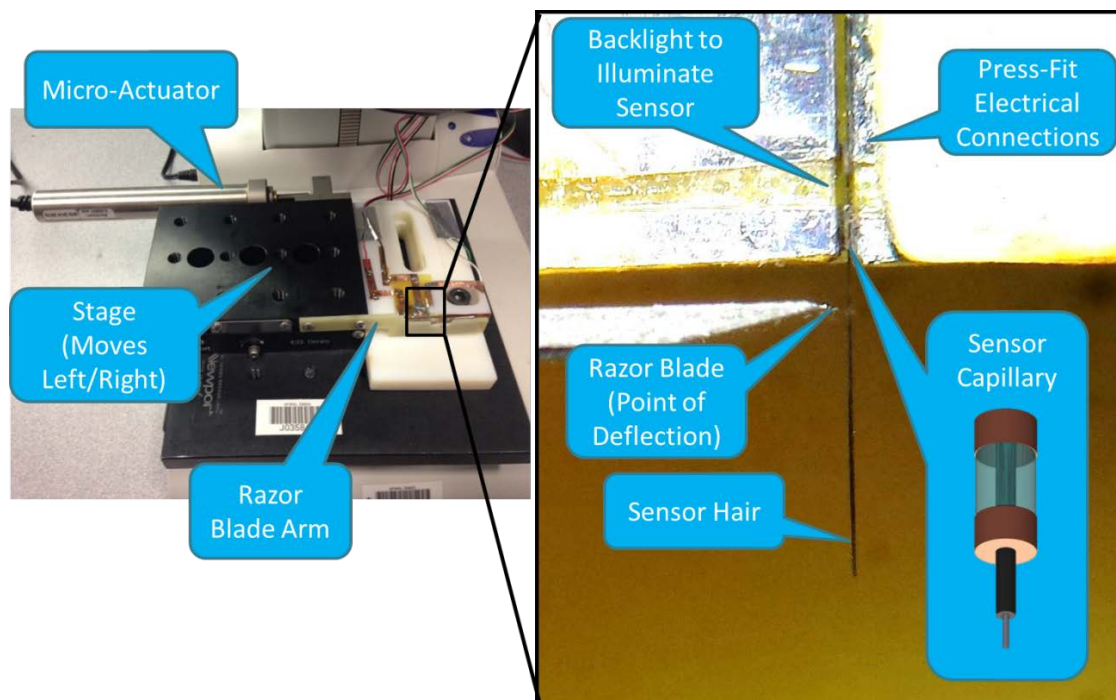
Figure 3. Benchtop Test Fixture for Hair Sensor Screening/Tuning/ Parameterizing

The response to point load for a typical sensor as it was deflected at various points (L_P = 600µm (23.6 mil), 800µm (31.5 mil), or 1,000µm (39.4 mil)) along the hair is shown in Figure 4. In all cases, the resistance decreases nearly sigmoidally with increasing deflection of the hair, which is similar to the response observed with increasing strain of planar nanotubes against a metal electrode. Up to about 60 µm (2.4 mil) of deflection, the sensitivity is low as the resistance change is nearly constant with increasing deflection. As the nanotubes at the opening of the capillary continue to be compressed against the metal electrode, the resistance decreases sharply before ultimately plateauing. The overall sensitivity decreases as the point load is moved farther from the base of the hair, as might be expected since the moment about the base of the hair is decreased. While the loading in airflow will be distributed over the hair, this point load response is somewhat analogous to the airflow response; that is, the average center point of the airflow along the length of the hair can vary as the boundary layer changes or as the hair length is altered.
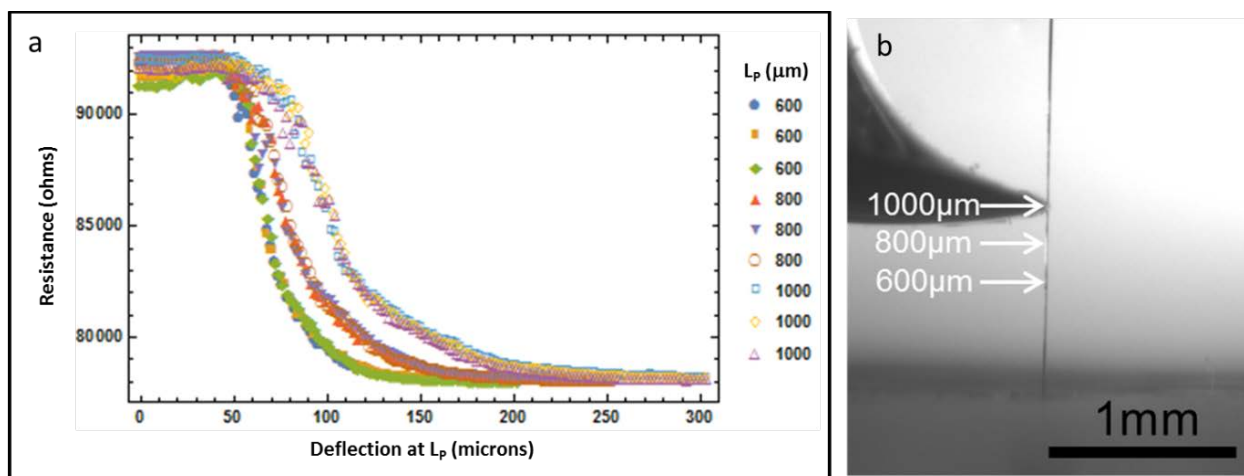
Figure 4. Typical Sensor Response to Applied Load and Illustration of Load Application

Note: (a) The response of a typical sensor to a load applied at 3 different points along the hair (L_P) as the deflection of the hair is increased each time. (b) Another point deflection apparatus with arrows indicating where the loads were applied to the hair.

While this baseline response to point loads can be obtained with minimal effort, it is already evident that the response differs with loading conditions thereby preventing direct extrapolation to their response to other loading conditions such as due to airflow. Models to accomplish this will be presented in the following sections, and here the properties of the sensor constituents needed to parameterize the models are listed as well as the methods for determining these properties. The glass fiber Young's modulus (E), radius (r), and density (ρ) are provided by the manufacturer as noted previously. With regard to airflow, the drag coefficient is proportional to the exposed length of the hair (L_E) and the diameter of the hair. This total hair diameter ($D(x)$) is increased over the glass fiber diameter by the additional length of the CNTs ($L_{CNT}(x)$), which varies along the length of the hair and can be measured optically as is L_E. As is discussed further in Section 3.3, the deflection response of the sensor is particularly dependent on the length of the CNTs at the base of the exposed hair ($L_{CNT}(0)$) or, in other words, at the opening of the capillary. The native properties of the nanotube array, namely the stiffness and the piezoresistivity, are of interest both for predicting the sensor response and for characterizing the typical properties of this novel material. Since it is not yet possible to directly or indirectly measure the piezoresistivity of the array, the electrical response of the sensor must be calibrated under known loading conditions (such as the point load response shown previously); however, it is shown in Section 3.3 that a typical value of the piezoresistivity can be determined from trends observed for many sensors. Finally, it is shown in Section 3.1.4 that the compressive modulus of the nanotube array (κ) can be determined from the mechanical response of the sensor.

3.1.4 CNT Compressive Modulus from the External Hair Deflection

Inside the capillary, the nanotube array supports the glass fiber. If the fiber is locally displaced at an axial position x from the radial center by a distance y, the nanotube array is compressed by the capillary wall and exerts a force per area on the fiber proportional to the compressive strain (ε_{CNT}) on the nanotubes, as described by

9

$$\kappa \varepsilon_{CNT}(\theta, y) \tag{1}$$

where κ is the compressive modulus of the nanotube array. This neglects shear forces on the array and assumes no adhesion to the sidewalls. A linear stress-strain relationship has been observed for compression measurements of nanotube arrays grown on planar substrates up to about 10% strain with values of κ ranging from 10 kPa (1.45 psi) to 10 MPa (1.45 ksi). [9,13,36] In the devices produced for this effort, the strain is a function of the angular location (θ) around the perimeter of the fiber, with the nanotubes directly in the path of the deflection experiencing the most strain. Defining this position of maximum compressive strain as θ = 0, the strain at θ for a given local deflection y is

$$\varepsilon_{CNT}(\theta, y) = \left(R + y\cos(\theta) - \sqrt{R^2 - \tfrac{y^2}{2}(1 - \cos(2\theta))} \right)/(R - r) \tag{2}$$

assuming the nanotube array is grown to the capillary edge ($L_{CNT} = R - r$). The nanotubes on the opposite side (270° > θ > 90°) experience little to no compression and are assumed to exert no force on the fiber.

Substituting Equation (2) into Equation (1) and integrating the force per area over the bottom half of the fiber perimeter gives the force per length (q):

$$q = \frac{\kappa r \pi y}{2(R - r)} - \frac{\kappa r}{(R - r)}\left[\sqrt{R^2 - y^2} - 2R + \frac{R^2}{y}\tan^{-1}\left(\frac{y}{\sqrt{R^2 - y^2}} \right) \right]. \tag{3}$$

For small strains (y << R), the second term of Equation (3) goes to zero, and q is linearly proportional to the displacement of the hair. Defining the stiffness constant k, the distributed load due to the nanotube array is

$$q(x) \approx ky(x) \text{ for } x < 0 \tag{4}$$

where

$$k \equiv \frac{\kappa r \pi}{2(R - r)}. \tag{5}$$

Therefore, the CNT array acts like a partial linear elastic base, supporting the hair below the capillary opening (x < 0), while the hair above the capillary opening is free and subject to external forces. The deflection anywhere along the hair can be predicted by solving the beam bending equation for these two regions and including the boundary conditions that the position and slope must match at the capillary opening. Boresi and Schmidt give the beam bending equation describing the bending of a semi-infinite beam supported by such a linear elastic base [37] (pp. 357-360)

$$y(x) = e^{\beta x}\left[C_1 \sin(\beta x) + C_2 \cos(\beta x) \right] \text{ for } x \leq 0 \tag{6}$$

where

$$\beta = \sqrt[4]{\frac{k}{4EI}} \tag{7}$$

using the boundary condition that the deflection of the hair goes to zero at negative infinity. The constants C_1 and C_2 are found by matching to the external profile of the hair as described previously. This is a good approximation for these devices, assuming that the external load is completely transferred to the nanotube array and that the deflection of the hair goes to zero far above the base of the capillary where the hair is fixed by epoxy. It is assumed that neither the CNTs nor the alumina significantly contribute to the bending stiffness (EI) of the hair.

A point load P, applied at a distance $x = L_P$ from the capillary opening, results in the following equations that meet the conditions described previously:

$$y(x) = -\frac{P}{6EI}x^3 + \frac{L_P P}{2EI}x^2 + P\frac{1+2L_P\beta}{2EI\beta^2}x + P\frac{1+L_P\beta}{2EI\beta^3} \text{ for } x \geq 0 \qquad (8)$$

$$y(x) = \frac{2\beta \exp(\beta x)}{k}[P\cos(\beta x) + L_P P\beta(\cos(\beta x) + \sin(\beta x))] \text{ for } x \leq 0. \qquad (9)$$

To characterize the compressive modulus of the CNTs within the capillary of a sensor, the external curvature of the hair with varying load is experimentally characterized and fit against the elastic base model above. To demonstrate this process, a point load was applied to the hair of a typical sensor (referred to as Sensor D1 in Section 3.4) at a position 950 μm (37.4 mil) from the capillary using the setup in Figure 3 to incrementally increase the deflection of the hair. Optical images of the resulting bending and displacement of the hair are shown for some of the ten applied loads in Figure 5a, and the profiles extracted from these images are shown in Figure 5b.
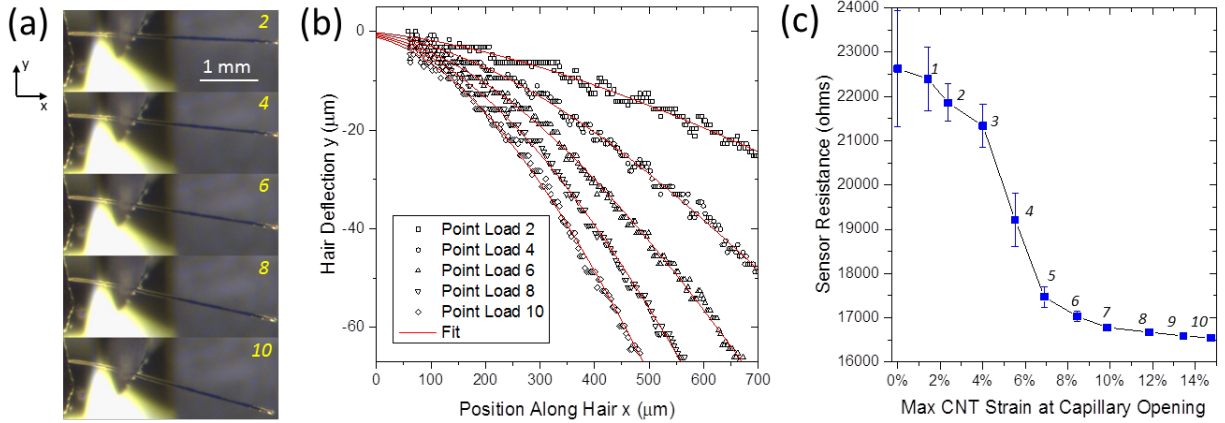
Figure 5. Illustration of Hair Response to Point Load

(a) Optical images of the hair in response to increasing point loads with indicated test number. The hair is partially obscured by the knife blade deflecting the hair. The capillary opening is to the left. (b) Profiles of the hair extracted from the optical images relative to the hair before deflection and the fit of the profiles to a static elastic base model. (c) The electrical response of the sensor to increasing load (numbered) plotted against the maximum strain experienced by the CNTs calculated from the fit results. Error bars are one standard deviation.

The resulting best fit of the deflections to the solution of Equations (1) and (2) are plotted with the corresponding optical images in Figure 5a. The coefficient of determination (R^2) of the fit is

0.996 with a stiffness constant k of 6.5 MN/m^2 (0.943 ksi). The electrical response of the sensor is plotted against both the deflection of the hair at the opening and the maximum strain experienced by the CNT array at the opening in Figure 5c The highest sensitivity is observed for strains at the pore opening of 2 to 8%, which is similar to the results reported for planar arrays.

For a stiffness constant (k) of 6.5 MN/m^2 (0.943 ksi), the corresponding compressive modulus (κ) from this relationship is 7.3 MPa (1.06 ksi).

3.1.5   Conclusions

Methods were demonstrated for fabricating, screening, tuning, and parameterizing hair sensors with structural microfiber hairs supported by CNT arrays that transduce the deflection of the hair into resistance. The sensors can be fabricated as individual units for easy distribution, or with batch (MEMS-free) processes for low cost manufacturing. The nature of the nanotube synthesis leads to reduced nanotube length within the capillary pore. The hair can be repositioned after the nanotubes are synthesized to bring the shorter nanotubes to the opening of the capillary for increased sensitivity.

The sensors typically exhibit a sigmoidal decrease in resistance in response to deflection, similar to the piezoresistive response observed when compressing nanotube arrays against a metalized electrode. In response to a point load, the resistance change with hair deflection decreases as the point load is moved away from the base of the hair. The sensors are parameterized by the length of the nanotubes along the hair (related to the expected drag coefficient of the hair), the length of the nanotubes at the opening (related to the sensitivity of the sensor), the length of the hair (related to the drag coefficient and bandwidth of the sensor), the stiffness of nanotubes (related to the sensitivity and bandwidth of the sensor), and the native piezoresistivity of the nanotube array (related to the sensitivity of the sensor). It is shown in Section 3.3 that the point load response can be used to calibrate the sensor in the absence of any method to characterize the CNT piezoresistivity.

As for the stiffness or compressive modulus of the nanotube array, it was demonstrated that the sensors can be modeled as a cantilever beam partially supported by an elastic base. The stiffness of this elastic base can be correlated to the compressive modulus of the nanotube array. The modulus measured for the sensor presented was 7.3 MPa (1.06 ksi), which is within (but at the upper end of) the range reported in literature [9,30,36] for arrays grown on planar substrates. This can be expected since inclusion of additional terms in Equation (3) and inclusion of additional forces from the nanotubes (shear, adhesion, etc.) would lower these estimated values of κ. The modulus of these CNT arrays could also be high since the planar measurements were for unrestricted nanotube growth, and the CNT arrays in the sensors are likely of higher density since the nanotubes were restricted to the volume of the capillary. While the compressive modulus is usual for comparing to other measurements of nanotube arrays, the β parameter in Equation (7) will be directly useful for calculating the forces and moments on the hair and expected deformation of the hair within the capillary.

3.2   CNT Synthesis in High Aspect Ratio Microcavities

3.2.1   Introduction

While there has been significant study of the growth and properties of CNT arrays on planar substrates and structural microfibers [9-20], there has been limited work on the synthesis of CNT arrays within confined geometries. For the CNT-based hair sensors described in this report, the

CNT array must be electrically continuous along the length of the fiber within the capillary, and the mechanical performance of the array as an elastic foundation for the fiber is in part determined by the dimensions of the array. During synthesis of the CNT array the nanotube growth products must enter from either end of the capillary in the space between the fiber and the capillary surface (less than 10 μm) and travel down the length of the capillary (around 1 mm). Similarly, composites reinforced or enhanced with CNT arrays require the growth of the CNT on woven fabrics of structural fibers where the spacing between fibers is a few microns and the spacing between fabric plies is around 25 mm. Growth between two closely spaced planar surfaces is envisioned of applications of the nanotube arrays as electromechanical interfaces or sensors. The high aspect ratio of such geometries could potentially represent a challenge in that the catalyst, carbon source, and synthesis conditions must all be present for robust growth of the self-aligned CNT arrays.

Growing the nanotube array to an optimum height at the pore opening is emphasized in Sections 3.1 and 3.3. In the following paragraphs, the relationship between the height and the length of the nanotubes within the capillary is described. As mentioned previously, the nanotubes near either opening of the capillary are almost as long as the nanotubes on the fiber external to the capillary, while the nanotubes near the axial center of the capillary are shorter. This difference in length is increased with increasing capillary length. One explanation for this observation is related to the diffusion of reactive gases into the capillary from the capillary ends; the reactive gases are consumed at the surface of the fiber and converted into nanotubes, which decreases their concentration towards the middle of the capillary. For these sensors, the nanotubes inside the capillary offer mechanical support to the fiber within the capillary, and they provide the electrical connection between the two ends of the sensor. The length of the capillary is important, since a short nanotube array will have a higher nominal resistance, while a long enough capillary will be an open circuit due to regions of no nanotube growth. While this application pushes towards continuity of the nanotube array within the capillary, it may be possible to use this restricted growth to realize tapered microstructures, such as tailored hair shapes, micro-antennae, brushes, or filters.

3.2.2   Methods, Assumptions, and Procedures

The CNT arrays are synthesized in a 25.4 mm (1 in) diameter quartz tube furnace reactor by a liquid injection method at atmospheric pressure. [38] The alumina coated fibers are inserted into the capillaries, and multiple fiber-capillary assemblies are placed on a graphite carrier substrate inside the tube furnace perpendicular to the direction of gas flow. Argon and hydrogen are flowed through the tube at 50 and 500 sccm (3.05 and 30.5 in^3/min), respectively, as the sample is heated from room temperature to 750 ºC (1,382 ºF); the maximum temperature is held constant during synthesis. Once the growth temperature is achieved, a 5% by weight liquid mixture of ferrocene suspended in xylene is injected continuously at a rate of 2 ml/hr (0.12 in^3/hr) into the tube furnace near the opening where the temperature is approximately 200 ºC (392 ºF). The gaseous products of the ferrocene/xylene vaporization flow with the Ar/H$_2$ gases to the devices. Forthe duration of the synthesis, the nanotubes grow nearly exclusively on the alumina coated surface of the glass fibers. The iron from the ferrocene forms iron nanoparticles on the growth surface, and each of these iron nanoparticles support the growth of a single multi-walled nanotube with additional carbon material at the iron nanotube interface (e.g. base growth). The nanotubes grow along the surface until a sufficient number are present to begin to lift-off the surface through mutual support. From there, the nanotubes grow as a partially entangled forest

or array primarily aligned vertically from the surface (radially from the fiber). The radial height of the array (h) is similar to but less than the length of the individual CNT lengths since the CNTs are wavy within the array. The nanotube array can be considered as a bulk material with density ρ_{CNT}. It is foam-like in its mechanical behavior [13,15,30,32] and about 3% dense by volume. [39,40]

The model for nanotube growth within the capillary is based on diffusion of the reactants and intermediates within the pore of the capillary and first order reaction kinetics on the surface of the alumina coated glass fiber. While the xylene and ferrocene mixture is generally assumed to break down into many reactive species at nanotube growth temperatures [38,41], focus was placed on the average behavior of the system. Therefore, a single diffusion coefficient (D_{eff}) and a single reaction coefficient (k'') is used. This average or effective diffusion coefficient describes the binary diffusive transport of the average reactive species relative to the remaining gases considered as a whole. The average reactive species is modeled for consumption at the surface of the fiber by a first order reaction at a rate proportional to the reaction coefficient k''. (The double prime follows the typical notation for a surface reaction with units of cm/s.) The identity of this reactive species is not the focus, but rather how these diffusive and reactive processes work together to create the CNT array profile within the capillary.

Outside the capillary, the concentration of the reactive species (c) is assumed to be constant and the height of the nanotube array (h) measured from the surface of the fiber is simply given by

$$h = \frac{ck''t}{\rho_{CNT}} \tag{10}$$

where t is the reaction time and ρ_{CNT} is the density of the nanotube array. Inside the capillary at any given time, the concentration varies down the length of the capillary and radially from the fiber surface. A second approximation that the radial variation in concentration is negligible compared to the axial variation can be made to further simplify the model. In this case, the system can be modeled as a one dimensional system in which the reaction at the surface can be thought of as existing throughout the open volume in the capillary. This volumetric reaction is proportional to the constant k''' with units of s^{-1} and is related to the surface reaction constant k'' by the ratio of the area of the reactive surface to the volume of the enclosed cavity:

$$k''' \approx \frac{A_{reactive}}{V_{enclosed}} k'' = \frac{b}{A} k'' . \tag{11}$$

Since the reactive area and enclosed volume share the same axial length L, the relationship reduces to the ratio of the cross-sectional perimeter of the reactive surface (b) and the cross-sectional area (A) of the enclosed volume. For the devices produced in this effort, A is the cross-section of the open space between the capillary wall (radius r_o) and the fiber (radius r_i), or $\pi r_0^2 - \pi r_i^2$, and b is the length around the perimeter of the alumina coated fiber, or $2\pi r_i$, since nanotubes do not grow on the capillary wall (Figure 6). It can also be seen in Figure 6 that this relationship will hold for any tube with continuous axial cross-section, taking into account the total reactive boundary. While the surface reaction constant k'' is independent of the dimensions of the system, the reaction constant for the projected volume k''' is expected to scale as the cross-section (e.g. capillary radius) is changed.
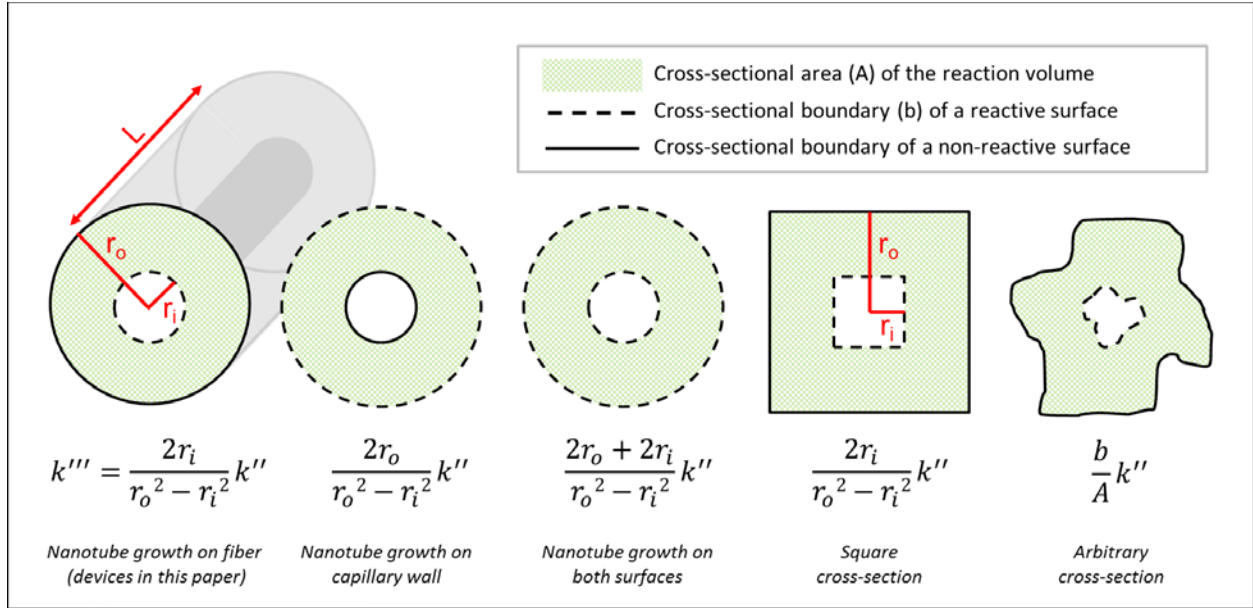
Figure 6. Cross-Sectional Schematic of a Glass Fiber Inside a Capillary

Note: A schematic of the glass fiber inside the capillary of length L is shown on the left. The open space between the fiber and capillary form a high aspect ratio tube for gas flow with cross section A (hashed green) between two circles of inner radius r_i (the fiber radius) and out radius r_o (the capillary radius). The nanotubes only grow on the alumina coated glass fiber, so the cross-sectional length of the perimeter of the fiber is the reactive boundary b. The surface rate of reaction is proportional to the reaction constant k'' and can be approximated as a homogeneous, volumetric reaction with reaction constant bk''/A or k'''. The relationship between k'' and k''' is shown for these devices, as well as for tubes differing in cross-section or combination of reactive boundaries (dashed line) and un-reactive boundaries (solid lines).

Assuming the effective diffusion coefficient and volumetric reaction constants do not change with time or concentration, the concentration profile inside the capillary is modeled by Fick's law in one dimension:

$$\frac{\partial c(y,t)}{\partial t} = D_{eff}\frac{\partial^2 c(y,t)}{\partial y^2} - k'''c(y,t). \tag{12}$$

The boundary conditions are similar to a classic Stefan diffusion tube [42,43]; the reactive species concentration at the openings of the capillary is assumed to remain constant throughout the reaction and zero inside the capillary at the start of the reaction. Since the concentration is constant, the height of the nanotubes at the opening is given by Equation (10). It is observed that the nanotube array height at the openings is not the same from sample to sample, so it can be assumed that the external concentration varies spatially inside the growth furnace, but remains constant in time. In this case, each end of the capillary experiences a unique constant concentration boundary condition, c_1 and c_2, and the solution to Equation (12) can be separated for the two openings:

$$c(y,t) = c_1 f_1(D_{eff}, k''', L, y, t) + c_2 f_2(D_{eff}, k''', L, y, t). \tag{13}$$

15

The height of the nanotube array after synthesis can be measured inside and outside the capillary, and is found from the model by integrating the concentration profile in the previous equation:

$$h(y,t) = \frac{c_1 k''}{\rho_{CNT}} \int_0^t f_1\left(D_{eff}, k''', L, y, t\right) dt + \frac{c_2 k''}{\rho_{CNT}} \int_0^t f_2\left(D_{eff}, k''', L, y, t\right) dt. \tag{14}$$

Using Equation (10), the unknown concentration, density, and surface reaction rate are replaced with the measured CNT heights at the openings h_1 and h_2:

$$h(y,t) = \frac{h_1}{t} F_1\left(D_{eff}, k''', L, y, t\right) + \frac{h_2}{t} F_2\left(D_{eff}, k''', L, y, t\right). \tag{15}$$

3.2.3 Results and Discussion

To test the model described in Section 3.2.2, nanotubes were grown for 180 seconds on fibers in capillaries of five different lengths and two different radii (r_o = 12.5 µm (0.492 mil) and r_o = 20 µm (0.787 mil)) during the same growth run. The resulting nanotube height profiles are shown versus axial position in Figure 7. While not smooth, the height profile is observed to be larger at the ends of the capillary than in the interior, as expected from the assumptions about the system; this difference is more pronounced with increasing capillary length. Interestingly, the nanotube array is not continuous from end to end in the two longest devices; these devices would be non-functioning since there is no continuous axial path for the current, even though the nanotubes are the ideal height at the openings. It can also be seen that the axial position of the height minimum is shifted towards the end of the capillary with the shorter nanotubes (e.g. Devices C and E), as expected for a difference in source concentration between the ends. Additionally, the nanotube growth is less in the capillaries with smaller radii as expected. For example, the near-zero-growth regions of the Device E are much smaller than Device D, even though the capillary is slightly longer. Note that the model does not account for any spatial heterogeneity of the growth that might be caused by non-uniform catalyst distribution or variation in growth efficiency.

Equation (15) was fit against all five of the nanotube growth profiles with $k_{12.5}'''$, k_{20}''', and D_{eff} as the three fit parameters, where the subscripts on k''' designate the value of r_o in µm. Even though the model can only predict a smooth profile, the resulting predicted height profiles (Figure 7 red curves) fit the measured profiles with a coefficient of determination R^2 of 0.9254, affirming the assumptions of the model for this confined geometry. For the predicted profiles in Figure 7, D_{eff} is 0.00025 cm^2/s (0.000039 in^2/s), and the corresponding diffusion length $(tD_{eff})^{1/2}$ is 0.21 cm (0.083 in). The k''' are plotted against the ratio $2r_i/(r_o^2 - r_i^2)$ per Equation (11) (Figure 7 inset). In agreement with the assumption of negligible radial concentration variation, the two k''' scale linearly and correspond to a k'' of 0.00014 cm/s (0.000055 in/s).
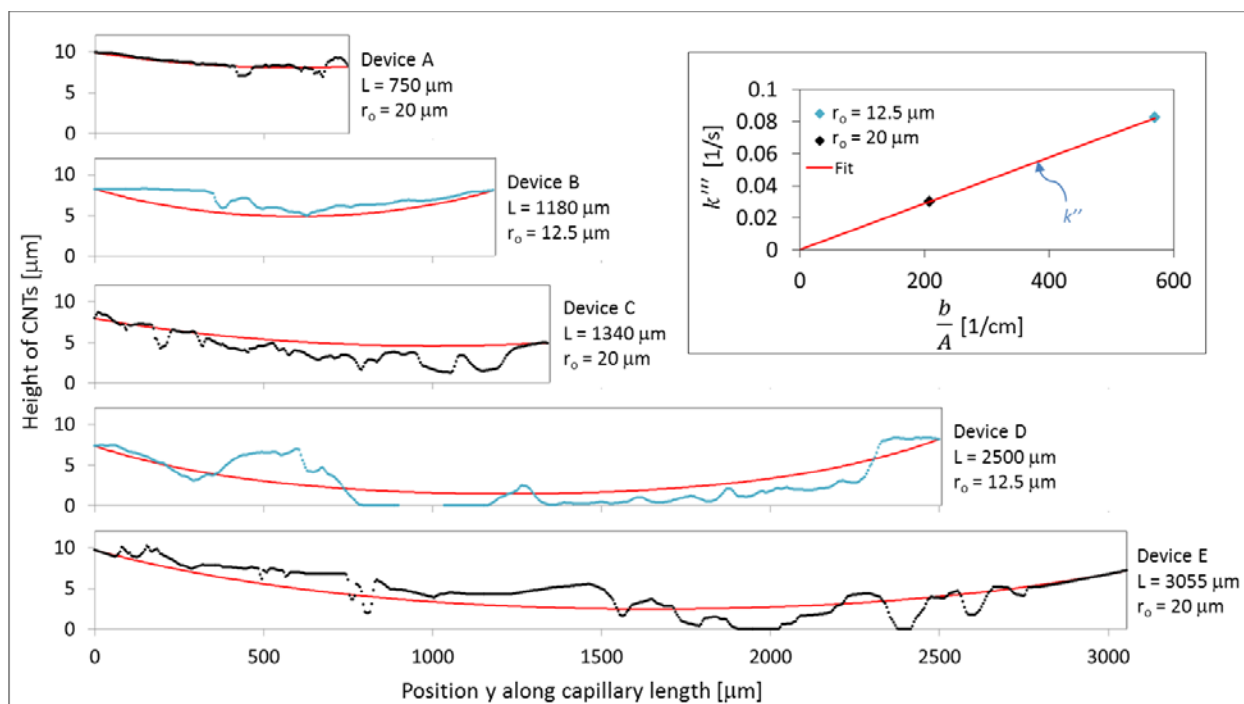
Figure 7. Nanotube Array Height

Note: The height of nanotube arrays grown vertically from the surface of alumina coated glass fibers of radius 4 μm (0.157 mil) inside capillaries with two different inner radii (r_o) and five different lengths, as noted. The time of the growth was 180 s. The red curves are the best fits to the model based on Fick's law with an average diffusion constant D_{eff} and an approximate volumetric reaction rate k''' scaled by the dimensions of the system to the surface reaction rate k''. The predicted profiles are the same and the R^2 is a maximum of 0.9254 for all $D_{eff} \geq 0.00025$ cm²/s (0.000039 in²/s). (inset) In example for $D_{eff} = 0.00025$ cm²/s (0.000039 in²/s), the best fit values for k''' for the two capillary radii scale linearly, as expected, with the ratio of the reactive cross-section perimeter b and the cross-sectional area of flow A. The slope, which corresponds to k'', is 0.00014 cm/s (0.000055 in/s) at this D_{eff}.

Plotting the R^2 from the fit versus the diffusion coefficient, it is seen that the R^2 increases up to a maximum of 0.9254 at $D_{eff} = 0.00025$ cm²/s (0.000039 in²/s), but plateaus rather than coming to a peak (Figure 8). The fit is just as good for all larger values of D_{eff}, suggesting that the values determined previously are the minimum possible values for D_{eff} and k''. Likewise, the reaction constant k'' corresponding to the best fit increases nonlinearly with D_{eff} up to the best-fit minimum D_{eff}, but then is approximately linearly thereafter. The CNT height profile appears to be uniquely dependent on the ratio of k'' to D_{eff}, but not on either value alone.
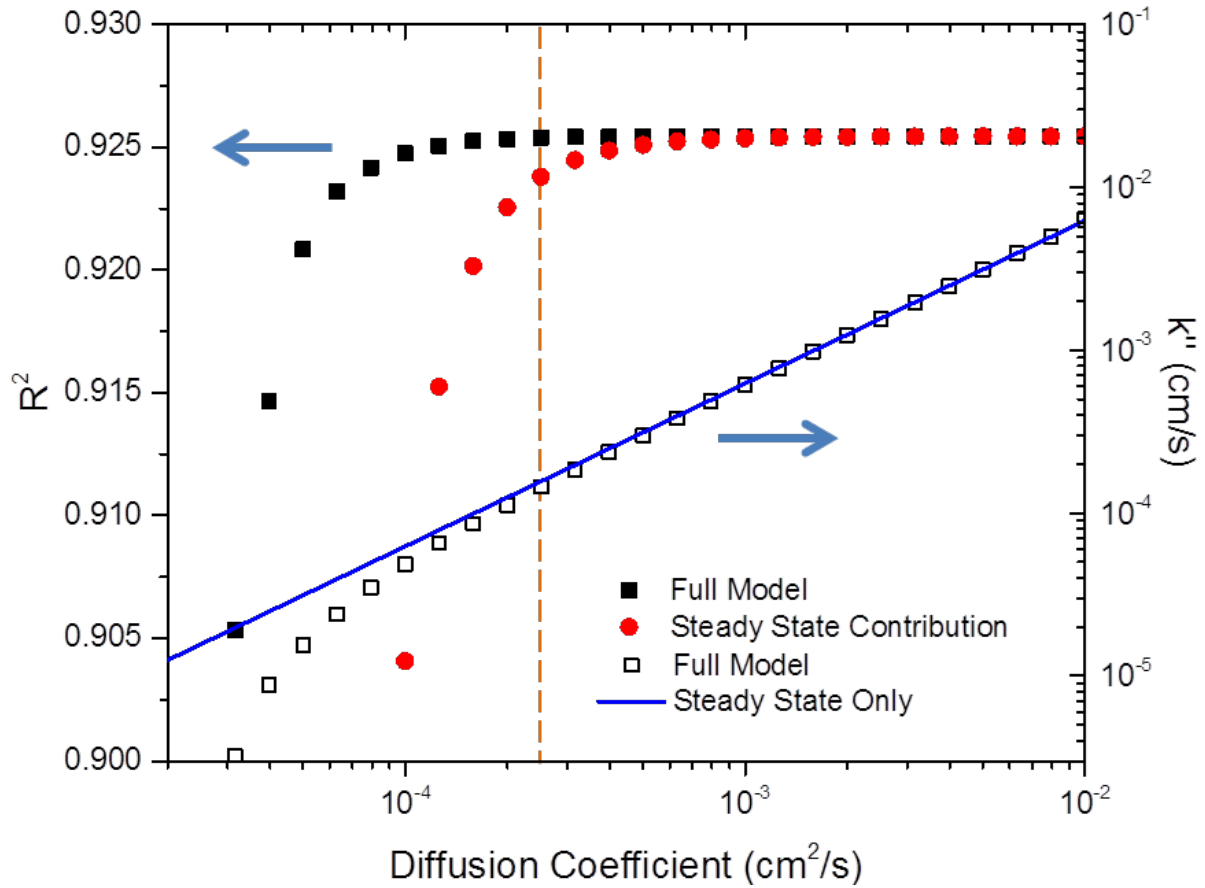
Figure 8. Coefficient of Determination and k" vs. Effective Diffusion Coefficient

Note: The coefficient of determination R^2 of the fit of the model compared to the measured CNT height profiles, and the k" corresponding to the best fit k''' parameters versus the effective diffusion coefficient D_{eff}. The R^2 is maximized at 0.9254, and the k" is linear for all D_{eff} greater than 0.00025 cm²/s (0.000039 in²/s), which is marked with a dashed line. The red circles show the fit to be almost as good using the same k''' and D_{eff} from the full model, but excluding the transient terms when calculating the predicted profiles. The blue line marks the k" found from the best fit to the model only considering the steady state terms. For the times required to grow the CNTs to fill the cross section at the opening, the reactive species concentration is at steady state over most of the growth duration, and the resulting height profile can be determined from the ratio of k" to D_{eff} found to be 0.624 cm⁻¹ (1.585 in⁻¹) under these growth conditions.

Looking again at the model, both the non-dimensional functions f in the concentration profile in Equation (13) have a time-independent, steady-state (SS) component and a transient (T) component

$$f(y,t) = f_{SS}(y) + f_T(y,t) \tag{16}$$

such that the integrated functions F in Equation (15) are likewise

$$F(y,t) = t f_{SS}(y) + F_T(y,t). \tag{17}$$

The steady state component for the first end is given by

$$f_{SS,1}(y) = \sinh\left((L-y)\sqrt{\frac{k'''}{D_{eff}}}\right) \bigg/ \sinh\left(L\sqrt{\frac{k'''}{D_{eff}}}\right), \qquad (18)$$

and $f_{SS,2}(y)$ has the same form with the L-y term replaced by y. While the dependence of the transient component on the reaction rate and diffusion coefficient is complex (not shown), the steady-state component of f is dependent purely on the ratio of k''' and D_{eff}.

Two analyses were performed to investigate the role of this ratio and steady state component. First, the data was fit against Equation (15), but with the transient term (F_T in Equation (17)) set to zero. In this scenario, the system reaches steady state instantaneously, approximately equivalent to the system reaching steady state quickly relative to the total growth time. The two ratios k'''/D_{eff} for the two different capillary diameters served as the two fit parameters, which in turn were used to determine k''/D_{eff}. The R^2 of the best fit is again 0.9254, corresponding to a k''/D_{eff} of 0.624 cm^{-1} (0.246 in^{-1}). After plotting a line with this slope in Figure 9, it can be observed that this ratio matches the slope of the linear k'' relationship to D_{eff} predicted by the full model.

The steady-state contribution was also assessed by calculating R^2 versus D_{eff} with the transient term again set to zero, but with the values of $k_{12.5}''$ and k_{20}''' previously determined from the best fit using the full model. For low values of the diffusion coefficient, the system takes longer to reach steady state, and the transient terms have a larger impact on the quality of fit. But, as D_{eff} increases above 0.00025 cm^2/s (0.000039 in^2/s), the steady state term dominates with a fit as good as the full model, as indicated by the same R^2 for all but the lowest values of D_{eff}. For synthesis of a nanotube array that nearly fills the cross section at the openings, it was concluded from these two results that the concentration profile of the reactive species along the length of the capillary is at steady state over most of growth period. Under these steady state conditions, the shape of the height profile is primarily determined by the ratio of k'' to D_{eff}.

Substituting k'' for k''' in $f_{SS}(y)$ using Equation (11) and moving the L under the square root, it can be seen that the height profile determined from the steady state concentration depends on the product of the two dimensionless ratios Lb/A and Lk''/D_{eff}. The first is essentially the physical aspect ratio of the system, taking into account the relative scale of the reactive surface. In the field of fluid flow, A/b is referred to as the hydraulic radius, where b is instead the wetted perimeter, and the flow velocity increases with increased hydraulic radius. D_{eff}/k'' also has units of length and can be thought of as the ability of the reactive species to move axially by diffusive forces against the competing reaction flux. Dividing the length by this value gives a dimensionless quantity referred to here as the chemical aspect ratio.
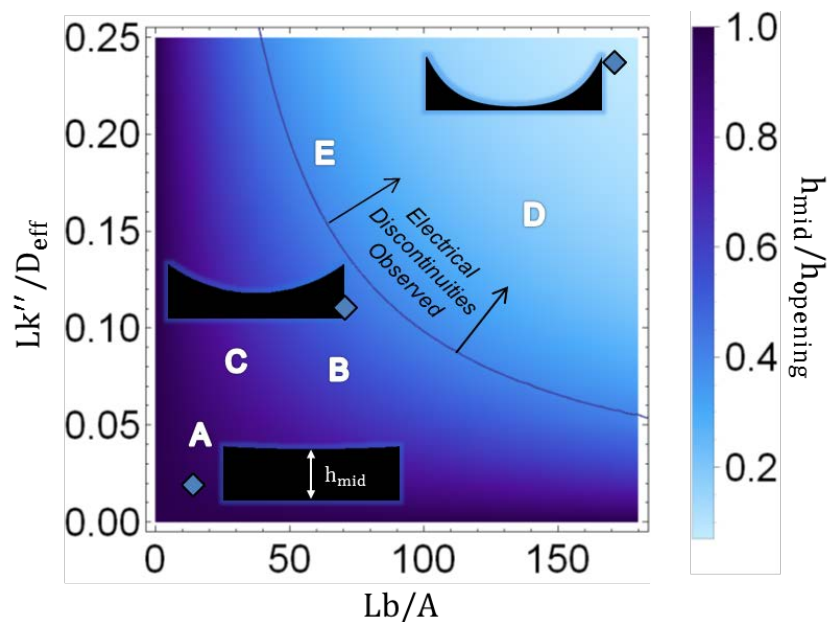
Figure 9. Predicted Nanotube Array Height

Note: The predicted nanotube array height – or total reaction product – at the midpoint per the nanotube height at the opening of a high aspect ratio tube versus the physical aspect ratio Lb/A and chemical aspect ratio Lk″/D$_{eff}$ from a steady state concentration profile. The white letters mark the values for the five devices characterized in this section. Using the values corresponding to the diamonds, three example height profiles with constant L are shown as insets ranging from nearly uniform along the length of the tube for lower values of the physical and chemical aspect ratios to highly tapered for larger aspect ratios. It is estimated based on experimental observations that regions of no growth (electrically discontinuous) occur when the predicted midpoint height is below about 40% of the height at the opening (marked as a line on the graph). Sensors above and to the right of this line are expected to have a high likelihood of being electrically discontinuous along the axial and of limited use for this application.

To show the relative impact of these factors in high aspect ratio reaction volumes, the predicted height of the nanotube array at the axial midpoint (h$_{mid}$) relative to the unrestricted height at the openings (h$_{opening}$) under steady state concentration conditions is plotted against a range of physical and chemical aspect ratios in Figure 9. For this calculation, the constant reactive species concentrations at the two openings c$_1$ and c$_2$ were assumed to be equal. In general, this height is equivalent to a measure of the total chemical surface reaction due to the reduced concentration inside the reaction volume relative to the total reaction that would take place over the same time period with the full source concentration. The five devices of Figure 7 are shown in Figure 9, as well as three example length-normalized profiles.

For low values of the ratios, the total reaction profile is seen to be nearly constant long the axial length, and the angle between the side and top of the profile is nearly π/2. As either ratio is increased, the height at the midpoint and the angle at the opening decrease, ultimately resulting in a highly tapered profile. While the model will never predict a zero height that would correspond to an electrical break, regions of no nanotube growth are typically observed when the predicted height at the midpoint is lower than approximately 40% of the opening height. This

line is marked in Figure 9 and corresponds to the longest capillary and highest degree of taper possible while still maintaining axial electrical continuity.

3.2.4 Conclusions

The CNT synthesis on the fiber within a capillary can be modeled and subsequently used to tailor the degree of taper of the CNT profile along the length of the fiber and within the capillary. In the specific case of the AHS, the axial resistance will be minimized for minimized capillary length and maximized h_{mid}, corresponding to low physical and chemical aspect ratios. A uniform nanotube array profile also corresponds to a more uniform elastic support for the hair within the capillary. However, for handling purposes, it is often desirable to maximize the capillary length while at least maintaining electrical continuity. As will be shown in Sections 3.3 and 3.4, it might be desirable to reduce the stiffness of the nanotube support to increase the deflection of the hair inside the capillary near the electrode at the opening. It may be possible to achieve this by reducing the quantity of nanotubes, such as from a highly tapered profile.

3.3 Structure-Property Relationships for Quasi-static Airflow Sensing

3.3.1 Introduction

While maintaining and manipulating differences in local airflow over the surface of an aircraft skin are critical to stable flight or agile maneuvering, conventional air systems operate without direct knowledge of flow conditions. In contrast, animals such as crickets, locusts, and bats are able to sense and quickly respond to external disturbances in the air or local separation of airflow. Artificial hair using CNTs are promising for their high sensitivity and ease of manufacturing, but the synthesis process produces variability between devices, and the properties of the nanotube array are not well correlated to synthesis conditions.

In the simplest case for using distributed sensors such as AHS, the sensors respond bi-modally in the presence or absence of a given stimuli, such as paints that change to another color above a certain temperature. For sensors that can vary proportionally to external stimuli, but perhaps not in a predictable way, a possible application method is to directly map the response of the sensor to the stimuli of interest. In the case of airflow sensors that would be distributed over a wing, it would be laborious to produce all of the loading conditions of interest for every sensor. Perhaps more viable in this case is to train a system via a neural network to interpret the response from a distributed array en masse. While the response of an individual sensor to a given stimulus is not necessarily known a priori in this case and may differ from sensor to sensor, the neural network will work best with sensors that are highly responsive over the expected range of stimuli and produce a repeatable response. In another mode of operation, it would be desirable to interpret the response of each sensor directly to know the forces acting on the hair, and then use that information to map changes in air flow. This brings the additional requirement of translating the response of the sensors into information of interest, which is made more challenging when sensors within a system are different. One option in this case is to calibrate the individual sensors directly to the stimuli of interest, or under well understood conditions that can be related to the stimuli of interest. A more desirable option is to be able to predict the response from the properties of the sensor, either determining these properties during the manufacturing process or measuring the properties post-fabrication.

Below is a discussion on the fabrication, characterization, and modeling of AHS with a piezoresistive CNT sensing element and structural glass microfiber hair. Much of the sensor is

enabled by self-assembled growth of the CNTs into an array that transduces the motion of the hair into changes in resistance, as well as serves as the compliant support for the hair. While CNT arrays have been studied on planar substrates, the electrical, mechanical, and physical properties of CNT arrays are still not well understood and are highly sensitive to the growth conditions. Moreover, while sensors such as these have been reported previously, how the properties of the CNTs are translated into the properties of the sensors has not been described well enough to predict sensor properties.

3.3.2   Materials and Methods

The sensors were fabricated according to Section 3.1.2, and the exposed hair length (L_E), the average diameter of exposed portion of the hair including the CNTs (D_{avg}), and the length of the nanotubes at the base of the hair ($L_{CNT}(0)$) were documented for each sensor. Point load measurements were conducted as described in Section 3.1.3. Airflow measurements were conducted in a square plane wave tube as described in Section 3.4.2

3.3.2.1   Stiffness of the Nanotube Array

The method and elastic base model described in Section 3.1.4 was used to determine the relative stiffness factor (β) for five typical sensors. The sensors were deflected at one or more points in the x-direction (along the hair) between 700 and 2,000 μm (27.6 and 78.8 mil) at various magnitudes in y (perpendicular to the undeflected hair) between 0 and 100 μm (3.94 mil). The resulting displacement of the hair between the capillary opening and the point load were optically characterized and fit to Equation (8). The point of the deflection L_P is known in each case, leaving one independent variable P per deflection and one variable β that was fit across all the deflections for a given sensor. The results are shown in Table 1. The high quality of the fit is indicated by the small errors for the fit parameter β and large R^2 values.

Table 1. Nanotube Array Stiffness Factor (β) and Compressive Modulus (κ) for Five Sensors.

Sensor	L_P μm (mil)	β 1/ m (1/f)	β Standard Error	R^2	K MN/m² (ksf)	κ kPa (psi)
1	768 (30.2)	6740 (2054)	65	0.996	0.23 (4.8)	260 (37.7)
2	977 (38.5)	10300 (3139)	94	0.999	1.2 (25.1)	1400 (203.0)
3	991 (39.0)	9310 (2838)	135	0.996	0.84 (17.5)	950 (137.8)
4	851 (33.5) 1120 (44.1) 1320 (52.0) 1410 (55.5)	9280 (2829)	59	0.997	0.83 (17.3)	940 (136.3)
5	820 (32.3) 1040 (40.9) 1320 (52.0) 1450 (57.1) 1630 (64.2) 1880 (74.0) 2070 (81.5)	6140 (1871)	18	0.997	0.16 (3.3)	180 (26.1)

The elastic base stiffness constant (k) and the compressive modulus (κ) were calculated from β using Equations (7) and (5), respectively. While all the calculated values of κ are within the range reported for planar CNT arrays, the nanotube array properties vary from device to device, as indicated by the order of magnitude differences in κ. This may be due in part to the variation in nanotube length within the capillary, since the model assumes the elastic base is axially uniform and radially continuous. Regions where the nanotubes do not grow to the capillary walls would result in a reduced apparent modulus, while overgrowth of the nanotubes would increase the array density and, likewise, the apparent modulus.

3.3.2.2 Drag Force on the Hair

For airflow sensing applications, the air exerts a distributed drag force on the hair. Assuming the flow-velocity is perpendicular to the undeflected longitudinal axis of the hair, the force per length due to drag at a position x above the capillary opening is

$$f_D(x) = \frac{1}{2}\rho C_D(x)D(x)[u(x)]^2 \tag{19}$$

where D is the local diameter of the hair (including the CNTs), u is the local velocity of the air, ρ is the density of the air, and C_D is the local drag coefficient, which depends on the Reynolds number

$$\mathrm{Re}(x) = \frac{D(x)u(x)}{\upsilon} \tag{20}$$

where υ is the kinematic viscosity of air. The diameter of the hair varies in x due to the non-uniform length of the nanotubes, but it was found that using a constant, average diameter (D_{avg}) is sufficient.

For small deflections of the hair, it is common to model the hair as an infinitely long cylinder for the purposes of determining the drag coefficient. Other than for $Re < 1$, a formula describing the relationship between C_D and the Re can only be found by curve-fitting to experimental measurements of drag coefficients for cylinders. For $Re < 20,000$, White proposes the relationship [44] (p. 210)

$$C_D(x) = 1 + 10[\mathrm{Re}(x)]^{-\frac{2}{3}}, \tag{21}$$

but for moderately small Reynolds number values ($Re < 500$), it was determined that the data is better fit with slightly different coefficients:

$$C_D(x) = 0.8 + 9.76[\mathrm{Re}(x)]^{-0.674} \tag{22}$$

When using this drag coefficient, a cylindrical cross section is assumed. For large deflections of the hair, the effective cross-section becomes elliptical, changing the drag coefficient.

3.3.2.3 Air Flow Profile

The Navier-Stokes equation can be solved with a Fourier series solution to determine the two-dimensional air velocity profile inside a rectangular tube, and from that the velocity profile at the mid-plane of the tube. The first few terms of the series are adequate to describe the axial velocity profile along the hair

$$u(x') \approx -\frac{56.9}{2}u_m\left[\frac{1}{8} - \frac{1}{2}\left(\frac{x'}{w}\right)^2 - \frac{4\cos(x'\pi/w)}{\pi^3\cosh(\pi/2)}\right], \quad x' = x - \frac{w}{2} \tag{23}$$

where w is the width of the tube and u_m is the mean of the velocity over the entire cross-section. The 56.9 multiplier is the same value that appears in the Darcy friction factor for square tubes.

3.3.3 Results

The response of a typical sensor to air flow in the square tube is shown in Figure 10(left). Similar to the piezoresistive response observed for planar CNT arrays, the resistance decreases from an initial resistance (R_0) as the average air velocity is increased and saturates or nearly saturates at a minimum resistance (R_{sat}). This sensor was tested in 4 test series over the course of 300+ hours. As can be seen in Figure 10, there is good agreement between the response at the beginning and end of each test series, even for durations as long as half a day. Comparing between test series, the sensor experiences drift over larger time frames, with both R_0 and R_{sat} changing independently. This sensor increased in resistance in each case, but other sensors have shown both increases and decreases in resistance over similar time scales.
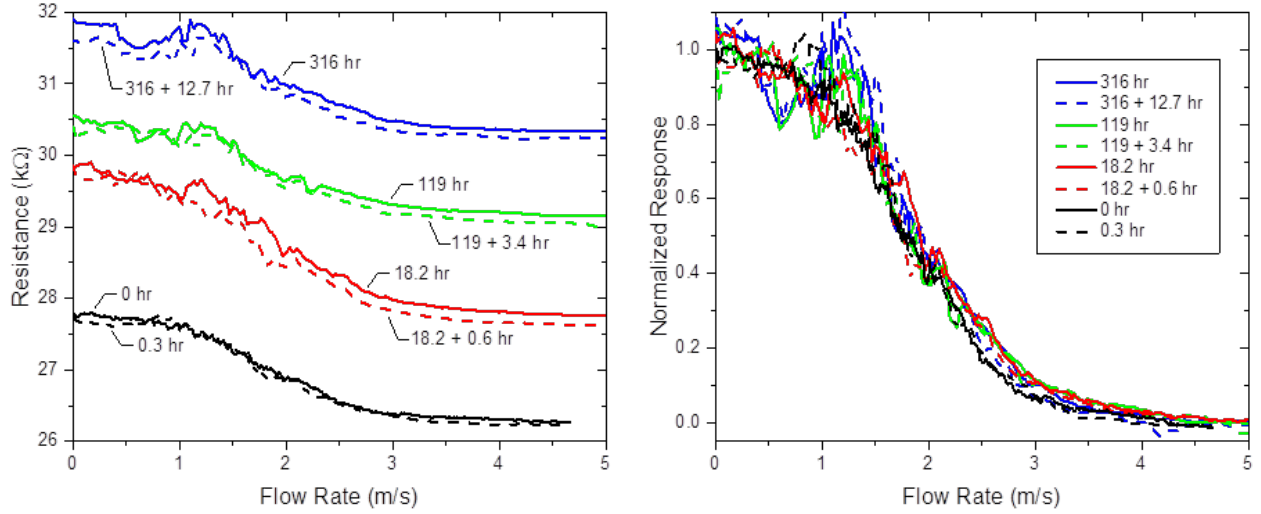
Figure 10. Stability and Normalization

It can be seen that the shape of the response is largely stable for the entire 2 weeks (Figure 10 (right)) by normalizing each curve to both R_0 and R_{sat} according to the relationship

$$R_{norm} = \frac{R - R_{sat}}{R_0 - R_{sat}} \qquad (24)$$

Small non-monotonic differences are still observed between the normalized response (R_{norm}) curves – especially at low air velocities – but the general, sigmoidal curve shape is maintained. In particular, the normalized slope of the linear transition region (approximately 0.4 s/m 0.12 s/ft)) and the air velocity (approximately 2m/s (6.6 ft/s)) corresponding to this region of maximum sensitivity are in good agreement between all the curves. This long term stability allows the response of the sensor to be compared under the various loading conditions presented here.

If R_0 and R_{sat} are assumed to be a function of the non-transducing regions of the device (electrodes and nanotubes deep in the capillary), it is also meaningful to compare the normalized response between devices. Figure 11 shows the response of five sensors to air flow in the square tube setup. Defining the sensitivity as the change in response per change in air flow, the sensitivity differs for each sensor even though they are of similar length. As can be expected and will be shown, the sensitivity for a given sensor should decrease with decreasing hair length since the cross section is reduced, but that trend is not observed in comparing these sensors. As shown in Table 1, the nanotubes differ in stiffness and length.
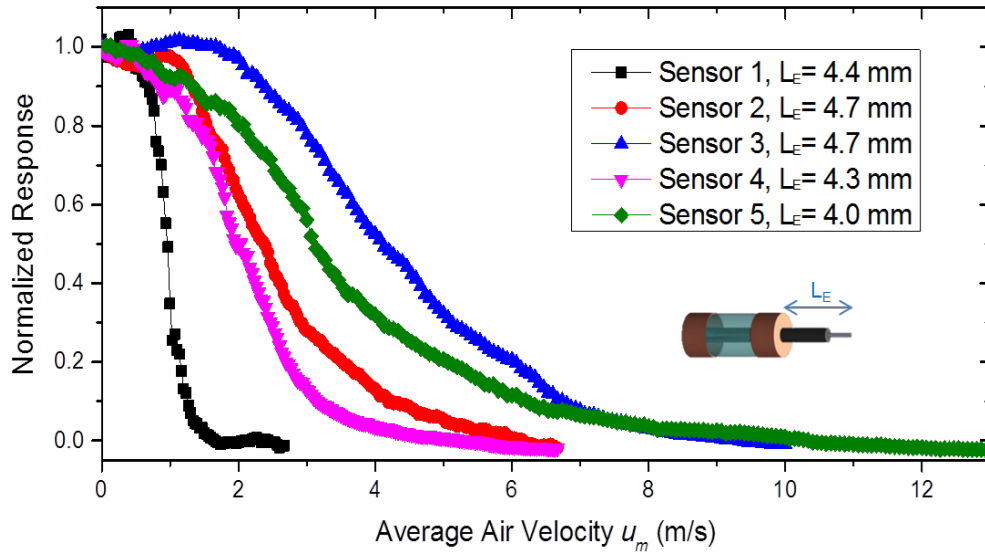
Figure 11. Air Flow Response of Five Sensors at Similar Exposed Hair Length

Figure 12 shows the normalized response of Sensor 4 as it was deflected at various points along the hair from 0 to 0.2 mm (0.0079 in). As expected, the sensitivity to deflection decreases with increasing distance from the base of the hair.
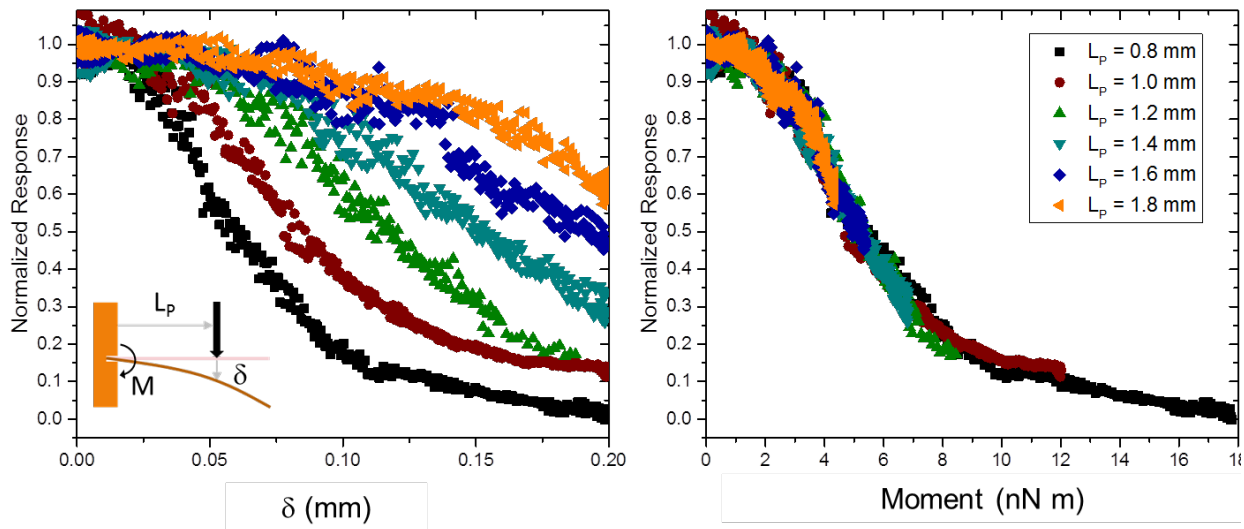
Figure 12. Normalized Response of Sensor 4 to Deflection at Various Points Along the Hair

The quasi-static responses of two sensors versus the mean air velocity in the square tube are shown in Figure 13. For each sensor, the response was collected at an initial hair length of approximately 4 mm (0.16 in). The hairs were then incrementally cut and retested to observe the change in response with decreasing hair length. As expected, as the length is reduced, the sensitivity to air flow decreases. The air velocity is zero at the top and bottom of the tube and is maximized at the center of the tube. For hairs longer than the midpoint of the tube (2.5 mm

(0.098 in)), the change in sensitivity with decreasing hair length is smaller than for hairs near or below the midpoint of the tube. As was seen in Figure 11, Sensor 1 is more sensitive than Sensor 4, and this behavior is preserved through all the hair lengths in Figure 13.
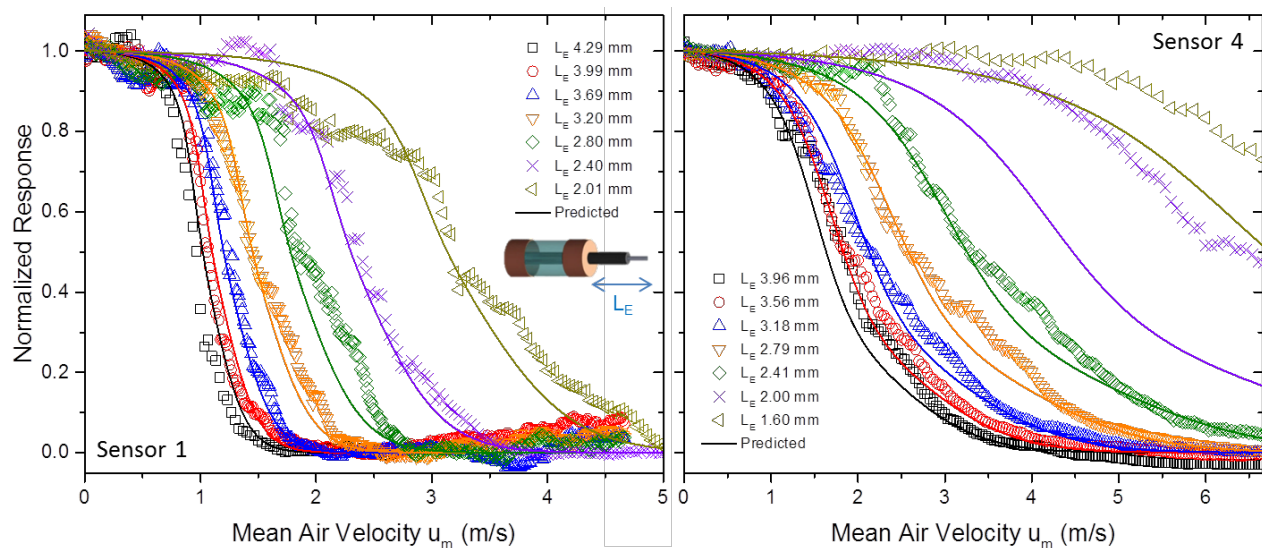
Figure 13. Discrete Data – Average Measured Airflow Response of Sensors 1 and 4

Note: The discrete data points indicate the average measured airflow response of Sensor 1 (left) and Sensor 4 (right) at multiple exposed hair lengths (L_E). The solid lines indicate the response predicted using the point load calibration curve and the moment calculated for each length of hair.

At higher airflows, the flow in the tube transitions from laminar to turbulent around a Reynolds number of 2,000, or an airflow of 6.4 m/s (21.0 ft/s). The response of three sensors of differing sensitivity and hair length are shown in Figure 14. Interestingly, the average resistance deviates from the trend observed under laminar flow conditions for each sensor, showing a decrease in sensitivity around Re = 2,000. More obvious and perhaps more expected for turbulent flow conditions, the RMS noise of the response sharply increases as the flow becomes turbulent.
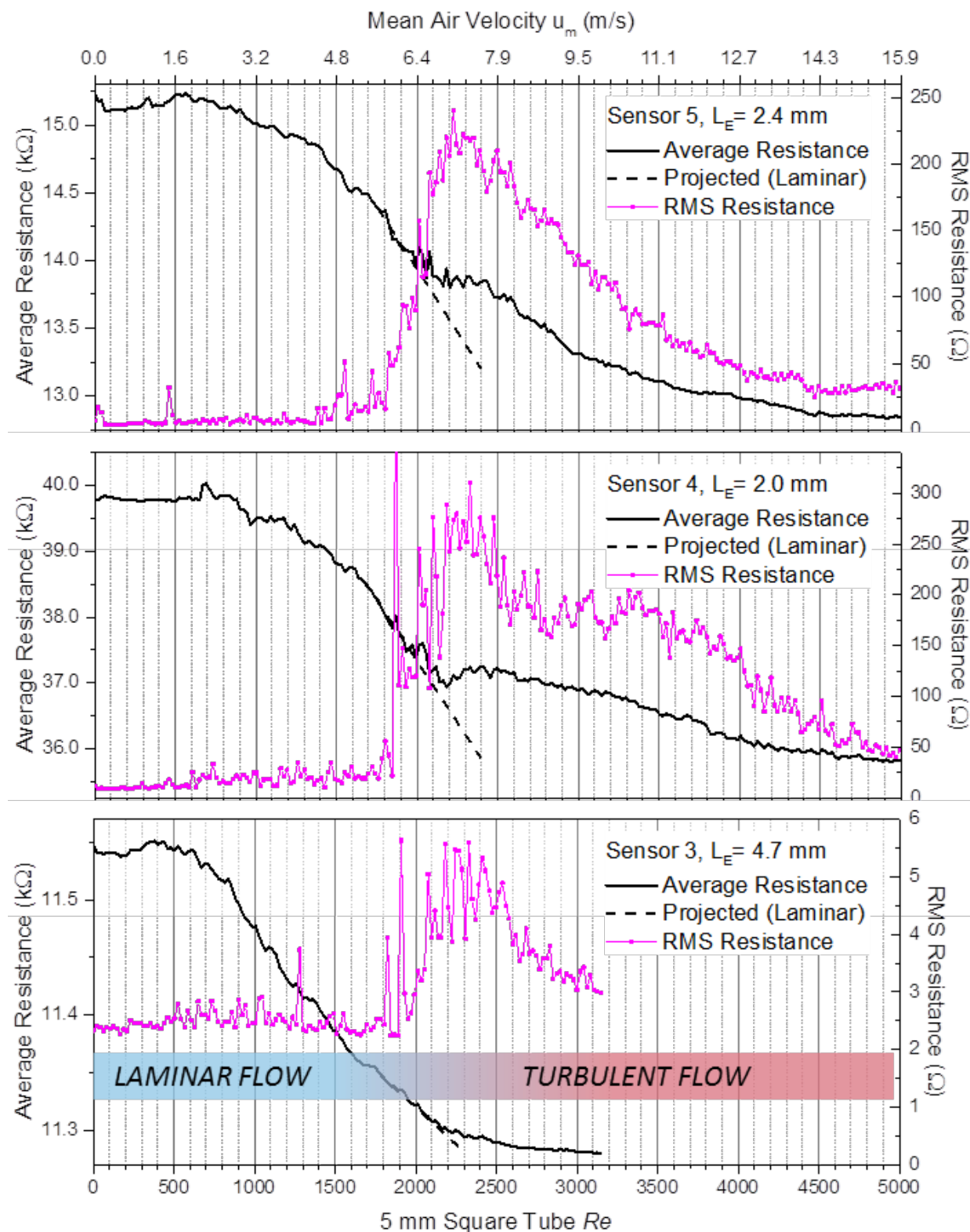
Figure 14. Sensor Response as Flow in the Tube Transitions from Laminar to Turbulent

3.3.4 Discussion

For planar arrays, a sigmoidal decrease in resistance similar to that observed for these devices has been reported with increasing compressive strain against a conductive surface. [9] This piezoresistive property of the nanotube array can be defined as the gauge factor (GF) with typical form

$$GF_{CNT} \equiv \frac{(R - R_0)/R_0}{\varepsilon_{CNT}} \tag{25}$$

where ε_{CNT} is the compressive strain on the CNTs, and the CNT subscript is used to designate these factors as properties of CNT arrays rather than the sensor. Since the change in resistance is not linear in strain, the gauge factor is not constant in strain and is maximized at some non-zero strain.

As the fiber is deflected in the sensors, the nanotubes within the capillary are compressed against the electrode in proportion to the local deflection of the fiber. As can be seen from Equation (9), this deflection is nearly zero throughout the capillary and is maximized near the opening (or base of the exposed hair). Since the change in resistance is a function of the strain on the CNTs, the response of the sensor should be dominated by the displacement of the hair at the opening (y(0)).

In the case of a point load, the displacement of the fiber at the opening according to Equation (8) is

$$y(0) = P \frac{1 + L_P \beta}{2EI\beta^3} \tag{26}$$

or

$$y(0) = -M \frac{1 + L_P \beta}{2L_P EI\beta^3} \tag{27}$$

where M is the bending moment about the capillary opening

$$M = -L_P P . \tag{28}$$

If L_P is much greater than $1/\beta$, then Equation (27) becomes

$$y(0) \approx -\frac{M}{2EI\beta^2} . \tag{29}$$

For forces on the hair far away from the capillary opening, the displacement of the hair at the capillary opening, and likewise the strain of the nanotube array, is proportional to the moment on the hair. As can be seen from Table 1, this should be the case for loads applied more than a few hundred microns from the exposed base of the hair.

Translating the deflection to moment in Figure 12 (right),

$$M = \delta \frac{6EI\beta^3 L_P}{3 + 6L_P\beta + 6L_P^2\beta^2 + 2L_P^3\beta^3} \tag{30}$$

where δ is the length of the applied deflection, the response curves fall on top of each other, confirming that the response of the sensors is proportional to moment, independent of the other loading parameters.

Since the air velocity goes to zero at the surface under laminar flow conditions, it can be expected that the majority of the drag experienced by the hair will also meet this condition, and the response of the sensor will generally scale with the moment. It is first necessary to determine the expected interaction of the air with the sensor and the air profile within the square tube to determine the moment on the sensor due to the airflow. Once the moment is known, it should be possible to use the point load results, such as the curve in Figure 12 (right), to predict the response to airflow.

The moment about the base of the hair due to drag is found by integrating the distributed drag force over the exposed length of the hair

$$M = \int_0^{L_E} x f_D(x) dx. \tag{31}$$

A common approximation that has been proposed is to treat the hair as a cylinder that has constant cross-section in length and width. The drag force in this case due to laminar air flow in the midplane of a square tube Equation (23) is given in Equation (19). The equation for the moment with this drag force must be solved numerically, and the predicted moment will be greater than the actual moment for large deflections of the hair.

The response predicted for Sensors 1 and 4 are shown in Figure 13. Given the length and average diameter of the hair, the expected moment about the base of the hair was calculated at each air flow. A calibration curve of the response to applied moment for Sensor 1 (not shown) and 4 (Figure 12 (right)) was determined from the point load response and measured CNT array stiffness for each sensor. The predictions show good agreement with the measured responses for all lengths of Sensor 1, from 2.01 mm (0.0791 in) to 4.29 mm (0.169 in) and for 0 to approximately 4 m/s (13.1 f/s).

Sensor 4 is less sensitive than Sensor 1 at the same hair lengths. There is good agreement for the five longest lengths of hair, but not for the hairs of length 1.60 mm (0.0630 in) and 2.00 mm (0.0787 in) for which the high sensitivity portion of their response curve starts above 4 m/s (13.1 f/s). It is possible that the baseline response was changed during handling or the process of cutting the hair down from 2.41 mm (0.0949 in); however, the overestimation of the sensitivity of the hair is consistent with the approximations made in modeling the drag force.

While the moment response differs from one sensor to another, it was shown that the expected response can be translated from one loading scenario to another if the magnitude of the moment is known in both cases. Looking towards incorporating large numbers of sensors into arrays for spatial flow mapping, it is feasible to envision calibrating their response by measuring the point deflection response of each sensor.

The only factor from Equation (30) that cannot be measured simply or easily from automated methods is β, or the nanotube array stiffness factor. While the process for determining β from the curvature of the deflected hair described earlier could be automated, it is not as feasible for large numbers of sensors; therefore, another method is presented here. Starting with the assumption that the response of the sensors is dependent on moment and independent of the loading parameters (for loads away from the base of the hair), the correct value of β is that which

forces the point deflection response curves for differing values of L_P (such as those in Figure 12) to collapse to the same moment response curve (as they do in Figure 12 (right)).

Going further, it is desirable to predict the sensor response purely from measurable quantities and, ultimately, to control for these properties during fabrication of the sensors to predetermine their performance. The sensors have been shown to have a characteristic response to moment, with a linear response near the point of maximum sensitivity (γ_{sensor})

$$\gamma_{sensor} \equiv \frac{\Delta R_{norm}}{\Delta |M|}. \tag{32}$$

It was suggested previously that the response of the sensor is primarily due to the strain of the nanotubes near the opening of the capillary, proportional to the ratio of the displacement of the hair and length of the nanotubes

$$\varepsilon_{CNT}(0) \approx \frac{y(0)}{L_{CNT}(0)}. \tag{33}$$

The change in resistance for a given strain is determined by the piezoresistive gauge factor of the nanotubes. Noting a similar sigmoidal response, the point of maximum sensitivity for the nanotube array normalized in a similar way is defined as

$$\gamma_{CNT} \equiv \frac{\Delta R_{norm}}{\Delta \varepsilon_{CNT}}. \tag{34}$$

Combining these equations with Equation (29), the normalized sensor sensitivity can be written as

$$\gamma_{sensor} = \frac{1}{2} \gamma_{CNT} \frac{1}{EI} \frac{1}{\beta^2 L_{CNT}(0)}. \tag{35}$$

which is a function of a known value (EI), two properties that can be measured (β and L_{CNT}), and one property that cannot yet be directly measured (γ_{CNT}).

Noting that the sensitivity should increase with decreasing nanotube length, 20 additional sensors ("HiS") were fabricated with shorter nanotubes. The point deflection response was collected at L_p values of 600, 800, and 1000 μm (23.6, 31.5, and 39.4 mil) for each sensor. The nanotube array stiffness factor β was determined by collapsing the point deflection response curves onto the same moment response curve as suggested earlier. The average length of the nanotubes at the capillary opening was 1.8 μm (0.071 mil), and the average β was 3050 m^{-1} (929 ft^{-1}) with an average standard error of 98 m^{-1} (29.9 ft^{-1}).

The normalized moment sensitivity for these 20 sensors and the five original sensors is plotted against the length of the nanotubes and β for each of the sensors, according to Equation (35) along with a linear fit, in Figure 15. Decreasing the length of the nanotubes increased the sensitivity by almost two orders of magnitude in some cases. The linear trend predicted is somewhat evident (R^2 of 0.72). The scatter may be due to the error in measuring the nanotube stiffness or length, or in the variation of γ_{CNT}.
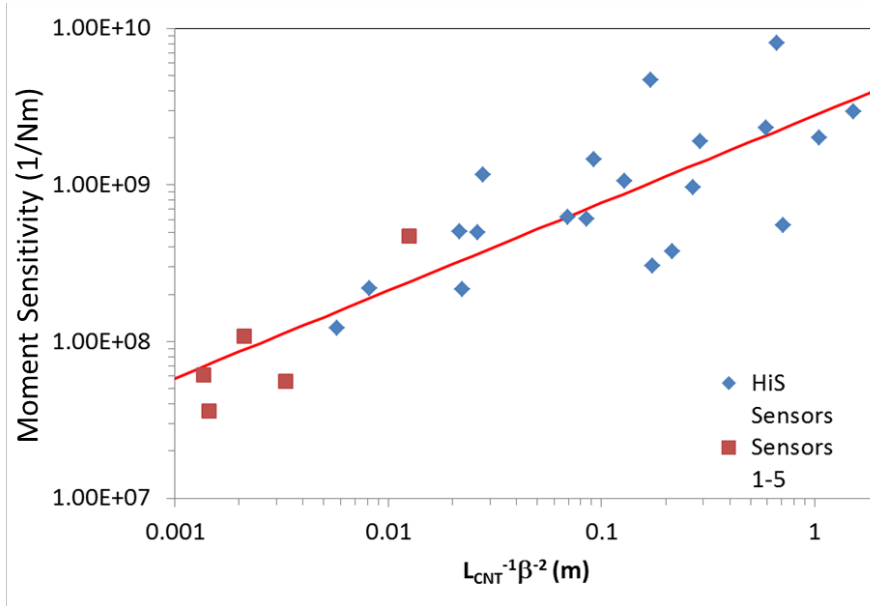
Figure 15. Normalized Moment Sensitivity vs. Nanotube Stiffness Factor and CNT Length

Note: The normalized moment sensitivity (γ_{CNT}) and linear fit for 25 sensors versus the nanotube stiffness factor (β) and the length of the CNTs (L_{CNT}) at the opening of the capillary.

Finally, the slope of the best fit line in Figure 15 corresponds to a γ_{CNT} value of about 0.6. Plugging this value back into Equation (35), it may be possible to predict the performance of future sensors without the need for calibration. While γ_{CNT} is related to the gauge factor, the normalization process removes information about the resistance values required to calculate GF_{CNT}.

3.3.5   Conclusions

It was demonstrated that the CNT growth process produces variability in CNT height, stiffness, and electromechanical sensitivity. The assembled sensor is moment-dependent and has a sensitivity that can be related to these properties with a linear expression. The sensor response in air flow can be directly estimated or calibrated using a benchtop deflection test. Results at higher airflows suggest a new potential application for sensors – detection of the onset of turbulence.

3.4   Dynamic Airflow Response

3.4.1   Introduction

The primary factors of interest for hair sensors include: (1) their detection threshold, the smallest amplitude of air perturbation that can be detected; (2) their sensitivity, or magnitude of response per change in air velocity; and (3) their bandwidth. [35,45,46] Regarding bandwidth, the sensor will give an in phase response to changes in airflow of frequencies typically ranging from DC to the first natural resonance of the system. For auditory or sonar applications of hair sensors and more exotic frequency-tuned air flow response schemes, the change in air flow at a specific frequency can be detected by instead operating the hair sensors at their resonant frequency or

with a collection of resonance-tailored sensors serving as a bandpass filter. [2,8,47] AHS are needed with tunable or maximized resonant frequency, while maintaining the sensitivity and detection threshold.

A number of AHS schemes have been developed, and the resonance properties have been reported for a few. Krijnen et al. suggest the product of the threshold and bandwidth as a figure of merit for hairs sensors. [46] Their SU8 hairs mounted on suspended membrane capacitors rotate at the base under air flow and exhibit a resonant frequency of 500 Hz for a 1 mm long hair. Chen et al. also use MEMS processes to fabricate 600 mm (23.6 in) long SU8 hairs on a silicon cantilever arm that resonate at 3.1 kHz. [48] Sarlo et al. make use of 2 mm (0.0787 in) long glass fibers embedded in a hydrogel root that exhibit both bending and rotation with a first resonance at 70 Hz. [49]

In this section, the operation of these nanotube-microfiber hair sensors is further described, and their response to changes in air velocities at acoustic frequencies is shown. The high stiffness per mass of the glass microfibers primarily results in a large bandwidth of operation, while the additional mass of the CNTs somewhat lowers the resonant frequencies from that predicted for a bare glass fiber. However, the resonant frequencies do not seem to be reduced by any contribution from the section of fiber supported by the CNT arrays inside the pore. These frequencies are shown to agree with those predicted for a beam partially supported by an elastic base with stiffness corresponding to the compressive modulus of the CNT array. They also agree with models that assume the hair is fixed at the transducer, suggesting the stiffness of the nanotubes is high relative to the mass of the glass fiber.

3.4.2   Methods, Assumptions, and Procedures

A 1 m (3.28 ft) long, 5 mm (0.197 in) square inner diameter aluminum alloy plane-wave tube connected on both ends to 8 m (26.2 ft) of copper pipe was used to expose the hairs to air flows at acoustic frequencies. A speaker driver (JBL 2446J, 16 ohms) was coupled into one end of the tube. The speaker was driven by a QSC GX3 power amplifier receiving a sinusoidal input signal from Stanford Research Systems SR 830 DSP Lock-In Amplifier. The signal measured by a Brüel & Kjær 4138 microphone mounted at the top of the tube at its lengthwise and widthwise center was fed to a 2670 preamplifier and recorded by the SR 830. A PID controller was used to adjust the output of the SR 830 to maintain a constant signal on the microphone. The sensors were mounted at the bottom of the tube directly below the microphone. The signals from the microphone and hair sensor were recorded by National Instruments Signal Acquisition Modules NI PXI-4472 (for the microphone) and NI PXI-6224 (for the AHS). The complete setup is shown in Figure 16. The assumption of purely propagating plane waves should be valid up to a cutoff frequency of about 34 kHz. [50]
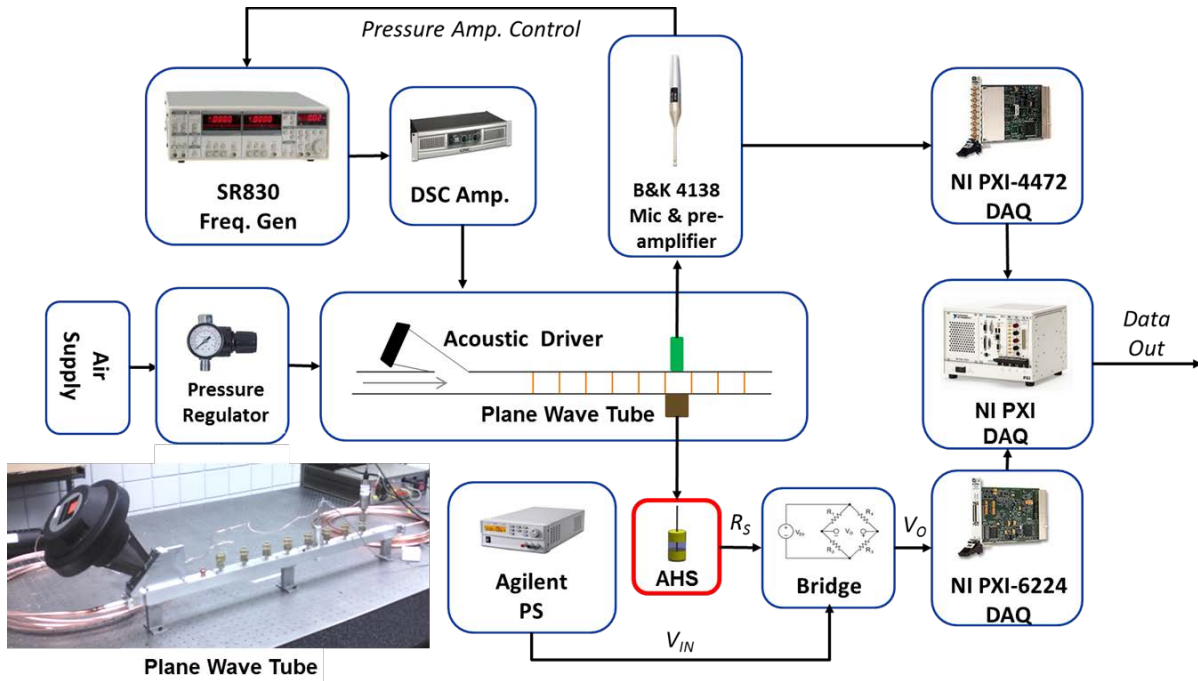
Figure 16. Hybrid Plane Wave Tube for Steady and Dynamic Air Flow Tests

The sound pressure (p_0) was measured at the same position along the tube as the sensor. The amplitude of the far field air velocity (U_0) can be calculated from the sound pressure assuming

$$U_0 = \frac{p_0}{u_s \rho_{air}}$$

(36)

where u_s is the speed of sound and ρ_{air} is the density of air.

CNT-based AHS were fabricated as described in Section 3.1. The sensors were each mounted in a polycarbonate disc which was machined to fit flush with the bottom surface of the plane-wave tube. A hole slightly larger than the outer diameter of the capillary was drilled in the polycarbonate substrate, which was previously metal-coated on one face. The sensor was positioned in the hole with the hair above the substrate and the top (exposed hair side) of the capillary flush with the top of the polycarbonate surface. Electrical connections were made between the substrate and the polycarbonate with silver epoxy, which also secured the sensor in the hole. Silver epoxy was also used to attach a wire to the bottom of the capillary.

Two typical sensors are reported in this section. First, the CNTs in the CNT Array of Sensor D1 (also discussed in Section 3.1.4) are approximately 20.5 μm (0.807 mil) long (total CNT-glass diameter of 50 μm (1.97 mil)), and the nominal resistance of the sensor was 20.1 kΩ. For Sensor D2, the CNTs were 12 μm (0.47 mil) long, and the nominal resistance was 5.2 kΩ.   The lengths of the hairs are noted in all cases and were measured to the nearest 0.01 mm (0.00394 in).

3.4.3   Results and Discussion

The response of Sensor D2 to a 300 Pa (0.0435 psi) RMS sinusoidal input signal at 100 Hz over 5 periods is shown in Figure 17a, as well as the Fourier transformed frequency response of the

sensor and microphone. While the input signal is one frequency, the sensor response is a mixture of integer multiples of the input frequency. This is consistent with the nonlinear, sigmoidal response observed for these sensors in their quasi-static response, but the absence of any other frequencies indicates that the sensor is only responding to the input signal. The response of sensor B to 350 Hz is also shown. At this frequency, the hair is in resonance with the input signal, as suggested by the large increase in magnitude of the resistance change. While the response is still nonlinear, as can be seen in the Fourier transform, the output of the sensor more closely matches the sinusoidal input.
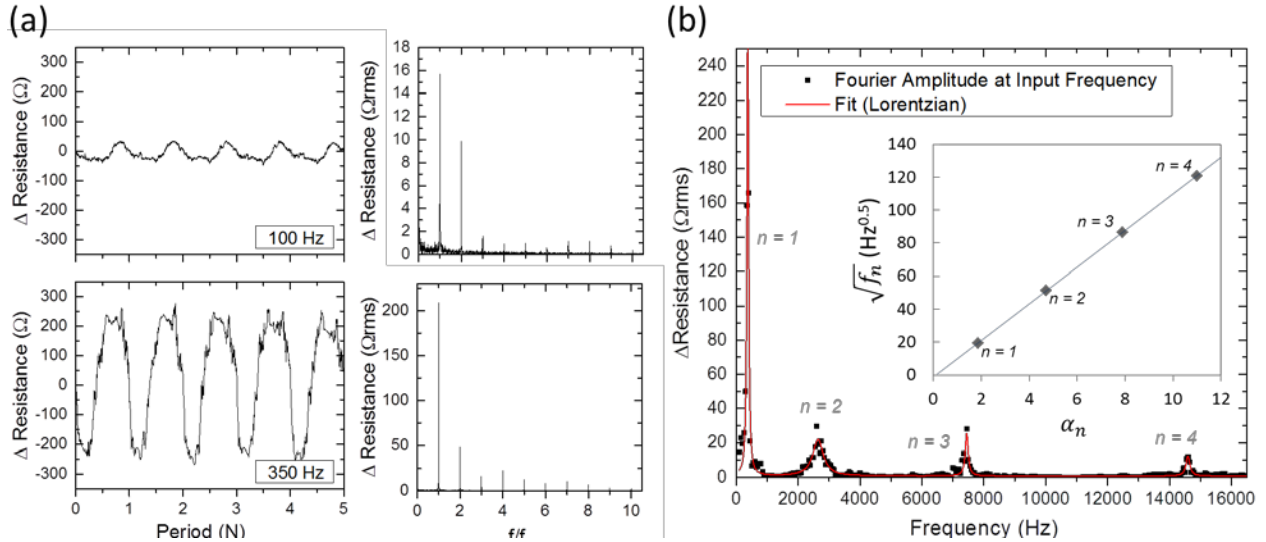
Figure 17. Response of Sensor D2 and Fourier Transformed Response

Note: (a) The response of Sensor D2 with L_E = 4 mm (0.16 in) at 100 Hz and 350 Hz over five periods and the corresponding Fourier transform versus the frequency divided by the input frequency f_0. (b) The amplitude of the Fourier transformed response at the input frequency versus the input frequency. The peaks correspond to the first four resonant modes of the hair sensor. (inset) The square root of the resonant frequencies (f_n) versus the amplitude factors of the fixed-free Euler-Bernoulli beam and a linear fit.

To resolve the natural frequencies of the sensor, the magnitude of the Fourier transformed sensor response at the input frequency was recorded as the frequency of the input signal was swept (Figure 17b). The first four resonant peaks can be distinguished, and each are well fit to a Lorentzian curve as is expected for a damped harmonic oscillator. The natural frequencies f_n for a vibrating Euler-Bernoulli beam are known to be

$$f_n = \frac{1}{2\pi} \frac{\alpha_n^2}{L^2} c \tag{37}$$

where

$$c = \sqrt{\frac{EI}{\rho A}} \tag{38}$$

assuming the bending stiffness (EI) and mass per length (ρA) do not vary along the length of the beam and where L, I, and A are the length, moment of inertia, and cross-sectional area of the beam, respectively. The α_n are determined from the boundary conditions of the beam. Assuming a beam that is free at one end (moment, shear = 0) and fixed at the other (slope = 0), the first four α_n are 1.875, 4.694, 7.854, and 10.996. Perhaps surprisingly, there is good agreement applying this simple fixed-free relationship to the data; the square root of the resonant frequencies can be seen to vary linearly with the fixed-free α_n (inset of Figure 17b).

To investigate the relationship between the vibrational response of the sensors and their length, the hair of Sensor D1 was incrementally reduced from an initial L_E of 4.37 mm (0.172 in) to a final L_E of 0.62 mm (0.024 in). The magnitude of the Fourier transformed response is plotted versus frequency in Figure 18a at each length. The first three resonant peaks are visible at the initial length, and each peak shifts to progressively higher frequencies as L_E is reduced, as expected. The resonant frequencies were extracted and are plotted versus the exposed length in Figure 18b. They are in good agreement with the inverse dependence on the square of the length predicted by the Euler-Bernoulli beam model. The bandwidth at any given length (e.g. 5.3 kHz at L_E = 1 mm (0.039 in)) is large compared to typical hair sensors.
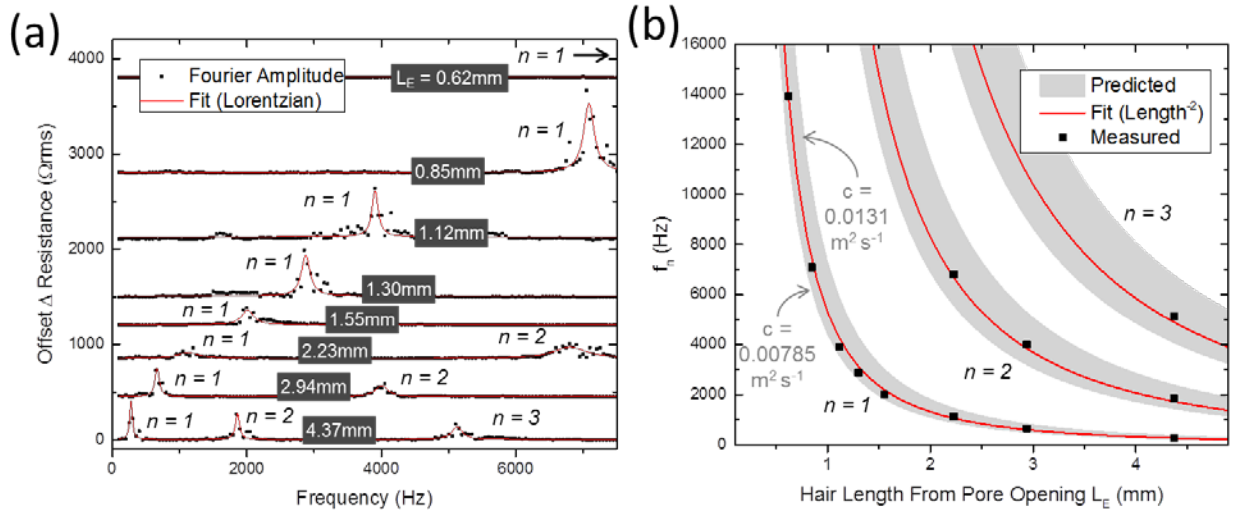
Figure 18. Fourier Transformed Response vs Length of the Hair

(a) The amplitude of the Fourier transformed response of Sensor D1 at the input frequency versus the input frequency for seven increments of L_E. The resonant peaks are labeled with their mode number, and they shift to higher frequencies as the length is decreased. (b) The resonant frequencies f_n versus the exposed length of the hair. Assuming the fixed-free model, the red fit curves corresponds to a value of c of 0.00946 m²/s (0.102 ft²/s), and the gray band shows the predicted frequencies for the glass fiber with a range of CNT masses.

For a fixed length of hair that moves in bending, it can be seen from Equation (37) that the resonant frequencies are proportional to the factor c – the square root of the ratio of the bending stiffness to the mass per length. Similarly, for hair sensors that rotate at the base, the resonant frequency is proportional to the square root of the ratio of the torsional stiffness of the hinge at the base of the hair to the mass per length of the hair. [46,51] The hair will move in rotation rather than bending as long as this torsional stiffness is small relative to the bending stiffness of

the hair. Therefore, in both cases, the bandwidth can be increased by choosing hair materials with large specific stiffness, and thus large c values.

For the glass microfiber used in these experiments, c is 0.0131 m^2/s (0.141 ft^2/s), as calculated from the reported E and ρ. It is expected to be reduced by the additional mass of the nanotubes. To determine the lower bound on c, the typical density of the CNT array (ρ_{CNT} = 0.5 g/cm^3 (0.0181 lb/in^3)) was estimated from mass and volume change measurements of CNT growth by the same method on large planar substrates. This density is somewhat larger than many reported values for CNT arrays since iron is continually fed to the system during synthesis, resulting in nanoparticles of iron through the volume of the array. The areal density is assumed to be preserved for the glass fiber, such that the additional mass per length on a cylindrical fiber is given by 2πrL$_{CNT}\rho_{CNT}$, and the predicted lower bound on c is 0.00785 m^2/s (0.0845 ft^2/s) for Sensor D1 and 0.00923 m^2/s (0.0994 ft^2/s) for Sensor D2.

The limits on c are compared to the values predicted by the fixed-free model in Equation (37) from the measured resonant frequencies. Using Equation (37) and assuming L to be the length of glass fiber outside the capillary (L = L$_E$ = 4 mm (0.157 in)), the value of c determined from the slope of the least squares fit in Figure 17b for Sensor D2 is 0.0121 m^2/s (0.13 ft^2/s) and within the range of predicted values. Again using Equation (37), the series of best fit curves for each mode across all the resonant frequencies for Sensor D1 in Figure 18b corresponds to a c of 0.00946 m^2/s (0.102 ft^2/s). These curves can be seen to fall within the gray band of predicted resonant frequencies from Equation (37) using the range of predicted c values for Sensor D1.

While a fixed-base model appears to accurately account for the resonant frequencies of the system, it does not provide insight into the mechanical role of the nanotubes supporting the fiber inside the capillary. Additionally, the fixed base model does not capture the operation of the sensor, since compression of the CNT array against the electrode by movement of the fiber at the opening (the "base") is neglected. Therefore, an elastic base scenario is again considered, this time adding a stiffness constant k to the time-varying Euler-beam equation:

$$EI\frac{\partial^4 y(x,t)}{\partial x^4} + ky(x,t) + \rho A\frac{\partial^2 y(x,t)}{\partial t^2} = 0 \tag{39}$$

where k is zero outside the capillary (x $\geq$ 0). This "partial elastic base" condition can be solved by treating the two sections of the beam independently and matching the solutions at the opening of the capillary. The resonant frequencies are found from the relationship

$$f_n = \frac{1}{2\pi}\sqrt{\left(\frac{\beta_n^2}{L^2}\sqrt{\frac{EI}{\rho A}}\right)^2 + \frac{k}{\rho A}} \tag{40}$$

where L is now the total length of the hair including the external length and the length of the capillary, and the β_n are determined from the boundary conditions. In this case for these devices, the hair is modeled as having a free end outside of the capillary and a fixed end at the bottom of the capillary.

In the absence of an elastic base (k=0), the β_n are identical to the α_n in Equation (37), and the natural frequencies are the same as those found from the fixed base model, but with L = L$_T$ rather than L = L$_E$. Eisenberger et al. predict that the resonant frequencies will be increased from these minimum frequencies if k is increased, trending asymptotically to the L = L$_E$ fixed base natural

frequencies. [52] The two models are equivalent for an infinite value of k in the elastic base model.

The response of Sensor D1, at an external hair length of 4.37 mm (0.172 in) and total length of 5.57 mm (0.219 in), to oscillating air flow with RMS sound pressure amplitude of 53 Pa (0.00769 psi) is shown in Figure 19a. Three peaks in the magnitude of the resistance change are observed, which correspond to the first three modes of the hair. The resonant frequencies are determined by fitting each peak to a Lorentzian curve, with the center of the fit peaks found to be at 273, 1872, and 5101 Hz, respectively. The resonant frequencies resulting from fitting to the fixed-base model are also indicated corresponding to a mass per length of 2.9×10^{-7} kg/m (1.95×10^{-7} lb/ft), which is within the predicted range.
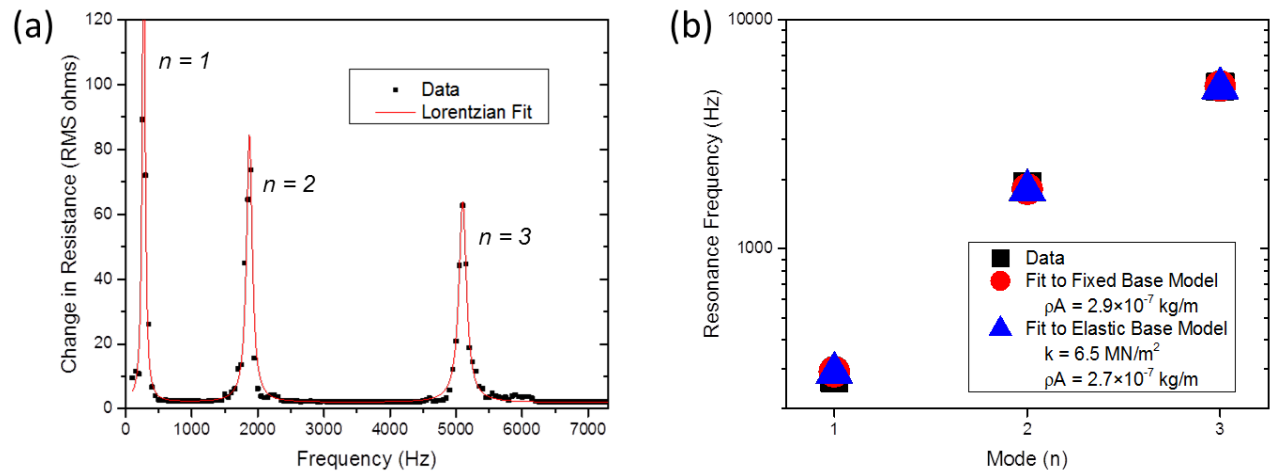
Figure 19. Resonant Modes – Amplitude and Measured/Predicted Frequencies

Note: (a) The amplitude of the response of Sensor D1 to varying frequencies of air flow at constant sinusoidal sound pressure amplitude. The peaks correspond to the first three resonant modes of the hair sensor. (b) The measured and predicted resonant frequencies versus mode number.

The fit of the resonant frequencies to the elastic base model is also shown in Figure 19b using the value of k (6.5 MN/m^2 (0.94 ksi)) obtained from comparing the deflection of the hair to a quasi-static elastic base model (Section 3.1.4) and with ρA again as the fit parameter. The mass per length (2.7×10^{-7} kg/m (1.8×10^{-7} lb/ft)) is slightly lower than the fixed base result, but still within the expected range. There is little difference between the resonant frequencies predicted from the two models and the measured resonant frequencies, which indicates that the sensors are at the asymptotic limit of the elastic base model, and the stiffness constant k is large relative to the mass per length of the hair.

Using the elastic base model, the predicted role of the nanotube stiffness in the resonant frequencies of the sensors is shown in Figure 20, keeping the other properties of the sensor identical to Sensor D1 and with L_E = 4.37 mm (0.172 in). As the stiffness is decreased, there is little change to the bandwidth (first resonance), even though the higher order modes show an obvious decrease in resistance.
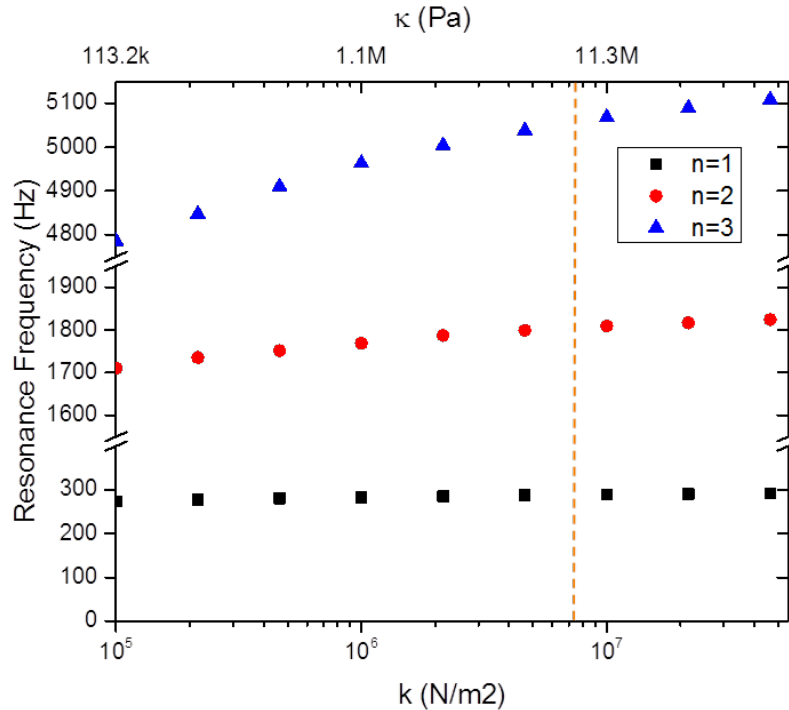
Figure 20. Predicted Resonant Frequencies

Note: The resonant frequencies predicted for the sensors for various nanotube stiffness values. The other properties of the modeled sensors are identical to Sensor D1 with L_E = 4.37 mm (0.172 in).

To assess the minimum detectable threshold of Sensor D1 (with L_E of 4.37 mm in this case), the amplitude of the response versus the measured sound pressure amplitudes (p_0) and calculated far field air velocity (U_0) at three different frequencies is shown in Figure 21a. The RMS noise level of the setup is observed to be approximately 2.9 Ωrms with no detectable change in resistance above this value for low air velocities. The resistance change increases linearly above an air velocity of 70 mm/s (2.8 in/s), which is taken to be the AC detectable threshold for this sensor with this measurement setup. Dividing the slope of this linear dependence by the nominal resistance of the sensor, the AC sensitivity is found to be 7.9 per mm/s (0.31per ft/s), similar to that reported for their static flow response. Whereas the bandwidth shows little dependence on k, the sensitivity and possibly the detectable threshold should be enhanced by decreasing the nanotube array stiffness.

For the shortest external length considered (0.62 mm (0.24 in)), the sensitivity is decreased, but the first-resonance bandwidth is greatly increased. The frequency of the sinusoidal plane wave was swept from 100 Hz to 16 kHz at a constant sound pressure amplitude of 300 Pa (0.0435 psi). The RMS change in resistance of the sensor is seen to be approximately constant with increasing frequency until the frequency approaches the first resonance of the sensor at 13.9 kHz and the response of the sensor reaches a peak (Figure 21b). A small peak is also seen around half this frequency, due to the increased contribution of higher modes of the input in the plane wave tube at integer multiples of the applied frequency. The response of 6 to 9 Ωrms below the resonance

is above the noise limit, making this a viable large bandwidth sensor even though the cross section is greatly reduced.

All else kept the same, it can be seen from the elastic base model that the bandwidth is approximately independent of the nanotube stiffness, while the quasi-static analysis in Section 3.3 indicates the sensitivity decreases as $k^{1/2}$. Conversely, the bandwidth and sensitivity have opposite dependence on the length and fiber bending stiffness, the former going as L^{-2} and $(EI)^{1/2}$, while the latter goes as L and $(EI)^{-1/2}$.
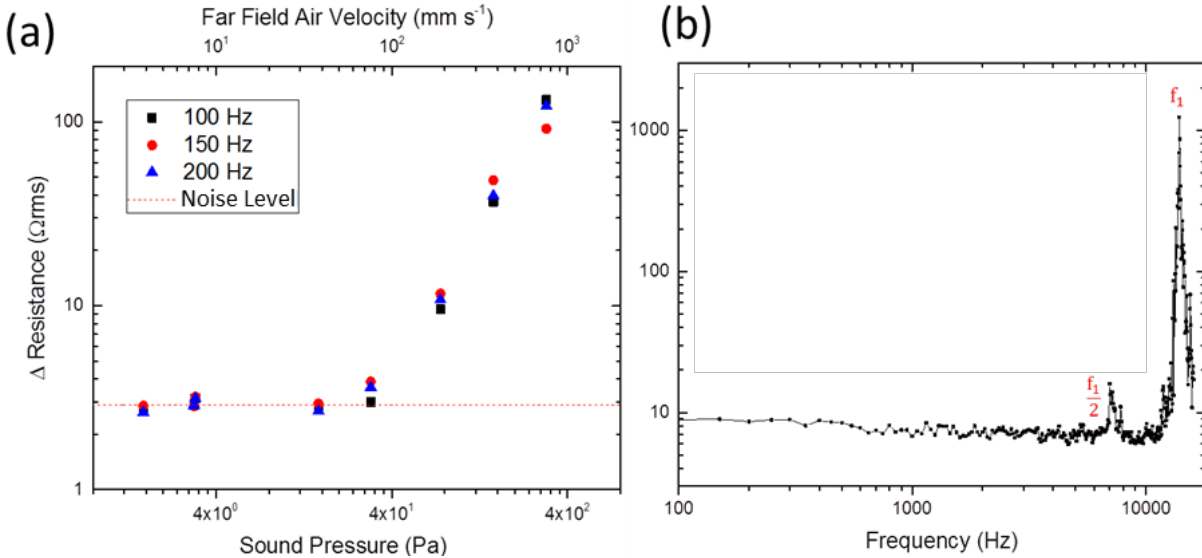
Figure 21. RMS Change in Sensor Resistance

Note: (a) The RMS change in resistance of Sensor D1 with L_E = 4.37 mm (0.172 in) from a nominal resistance of 20.1 kΩ to varying sound pressure or air velocity. The noise level is seen to be 2.9 Ωrms. The response increases linearly for air velocities above 70 mm/s (2.8 in/s) at a normalized rate of 7.9 per mm/s (0.31 per in/s). (b) After reducing the L_E to 0.62 mm (0.024 in), the first resonance f_1 is increased to 13.9 Hz, and the resistance change is seen to be nearly constant with changing frequency up to the resonant frequency. An additional peak is seen at half the resonant frequency due to the increased presence of higher modes within the plane wave tube at these frequencies. The minimum of the graph is 3 Ωrms.

3.4.4 Conclusions

The large specific stiffness of the glass microfiber enables these sensors to be tuned over a large range of frequencies or to operate over a large below-resonance bandwidth. The nanotubes serve to mechanically position the glass fiber within the capillary pore during synthesis and to suppress the vibration of the fiber base during operation. The deflection of the fiber at the base is small enough for the glass fiber to resonate purely in bending as if fixed at the opening of the capillary, maximizing the bandwidth. It has been shown that this can be accounted for by the large native compression stiffness of the nanotubes relative to the low mass of the glass fiber, yet the fiber is deflected at the opening of the capillary enough to produce a large change in resistance even at small air velocities.

The mass of the iron-rich CNTs on the external portion of the fiber appears to account for the slightly lower resonant frequencies and stiffness-to-mass factors c than would be predicted for bare glass fibers. While expected, the shift in these properties was not as large as predicted. For example, the measurements of the resonant frequencies of the hair were used with the fixed-free model to calculate a c of 0.00946 m^2/s (0.102 ft^2/s) and a c of 0.0119 m^2/s (0.128 ft^2/s) with the elastic base model, but neither value was as low as the c of 0.00785 m^2/s (0.0845 ft^2/s) predicted purely from the additional mass of the nanotubes. Better methods for determining the density of the CNT array would allow for better estimates of the CNT mass contribution. The CNT array could also act to increase the bending stiffness of the hair, which would increase c.

This combination of high specific stiffness fiber and CNTs with the appropriate amount of stiffness contributes to the record-high DC sensitivity shown previously, and the high AC sensitivity shown here. While not the lowest detectable threshold, most of the envisioned applications operate well above 70 mm/s (2.8 in/s). Future efforts will take advantage of the predicated ability to change the sensitivity independent of the bandwidth through the properties of the nanotube array.

3.5   Mechanical Shear Sensing

3.5.1   Introduction

Many of the advantageous qualities of the sensors for air flow detection, including small volume, low power consumption, ability to be distributed, are also attractive for mechanical sensors that can be embedded in structural materials such as composites. Below is an introduction to a new application for these deflection-based sensors as shear sensors by embedding a sensor within a bonded composite and measuring the displacement between adherends in a lap shear test. [21]

3.5.2   Methods, Assumptions, and Procedures

Lap shear coupons 25.4 mm (1 in) wide were prepared by bonding two pieces of 1.61 mm (0.0633 in) thick fiberglass epoxy composite adherends (Sabic G10/FR4) with an epoxy adhesive (Hardman Red #04001). Wire spacers in the bond were used to define an adhesive thickness of 0.254 mm (0.01 in) (Figure 22c). A small hole was drilled through the thickness of the adherends in the bond region for inserting the sensor. The hole radius was 0.286 mm (0.0113 in) through most of the thickness, but narrowed to 0.171 mm (0.00673 in) at the bond line to provide a stop for the top edge of the capillary and provide a contact point for the hair (Figure 22a).

A CNT-based hair sensor was fabricated and characterized as described in Section 3.1. The response of the sensor to point loads applied at 1 mm (0.04 in) from the capillary opening was characterized (not shown), so the same contact point was chosen within the coupon. Small wires were attached to the top and bottom electrodes of the sensor before inserting it (Figure 22b).
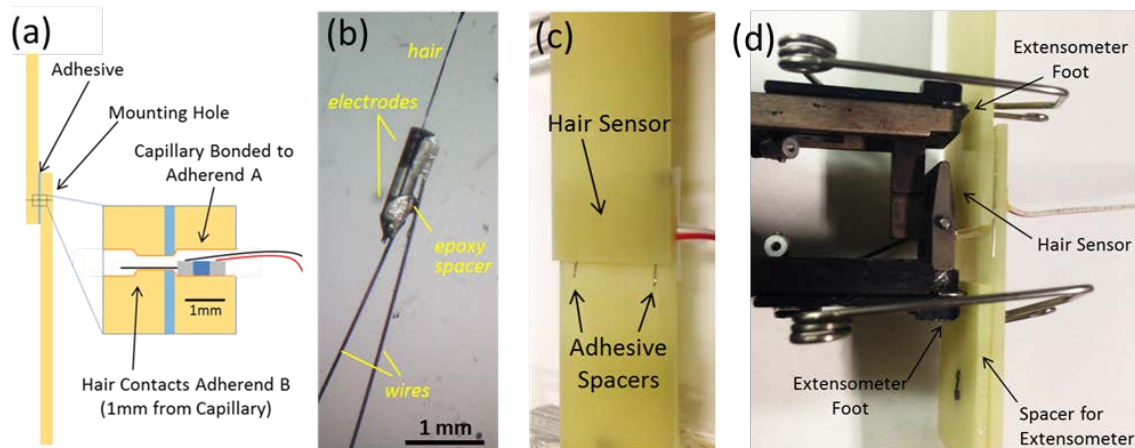
Figure 22. Embedded Hair Sensor – Schematic and Optical Images

Note: (a) Cross-section schematic of the lap shear coupon and embedded hair sensor. (b) Optical image of the hair sensor. (c) The lap shear coupon with embedded hair sensor. (d) Side view of the coupon with extensometer.

3.5.3   Results and Discussion

For mechanical testing, the sample was loaded in tension to 1,020 N (229.3 lbf) and then cycled at a rate of 0.05 Hz between 270 N (60.7 lbf) and 1,780 N (400.2 lbf), or approximately 10% to 67% of the expected maximum load. The signals from the load cell, an extensometer mounted with a foot on each adherend, and the hair cell are shown in Figure 23, and the cyclic load is evident in the response of all three.
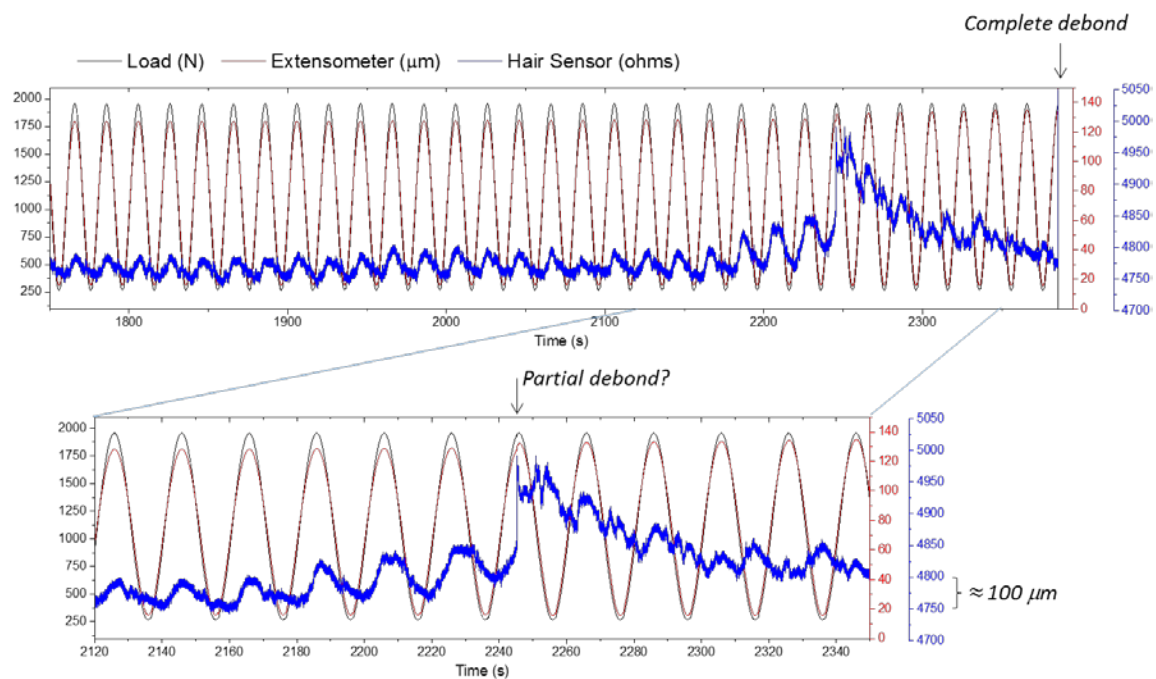
Figure 23. Applied Cyclic Load and Response from the Extensometer and Hair Sensor

Note: (bottom) The response near sample failure.

This sensor showed an increase in resistance with deflection under point load testing before embedding into the lapshear coupon, and once embedded it likewise shows an increase of about 10 ohms over each load cycle for the first 15-20 cycles. Comparing this to the point load calibration, this corresponds to about 100 μm of displacement. The extensometer likewise shows about 120 μm (4.72 mil) of maximum displacement over these cycles.

As can best be seen in the zoomed in section of Figure 23, the hair sensor increases in average resistance from around 2170 seconds before peaking around 2245 seconds, indicating that the sample is increasing in average displacement with each load cycle. This amplitude increase could be an indication that the adhesive is beginning to weaken. The sharp increase at 2245 seconds might be due to a partial debond of the sample before it ultimately fails (complete debond) around 2350 seconds.

Figure 24 shows the deviation in response of the load cell, extensometer, and hair sensor using the 15 cycles before 2100 seconds as the reference. In this view, the anomaly at 2245 seconds is apparent in all three. Similar to the hair sensor, the extensometer shows an increased amplitude for the 3 or 4 cycles leading up to a sharp increase at the anomaly. Differing from the hair sensor, this change in response is much smaller than the amplitude of response observed over the reference timeframe (Figure 24d).
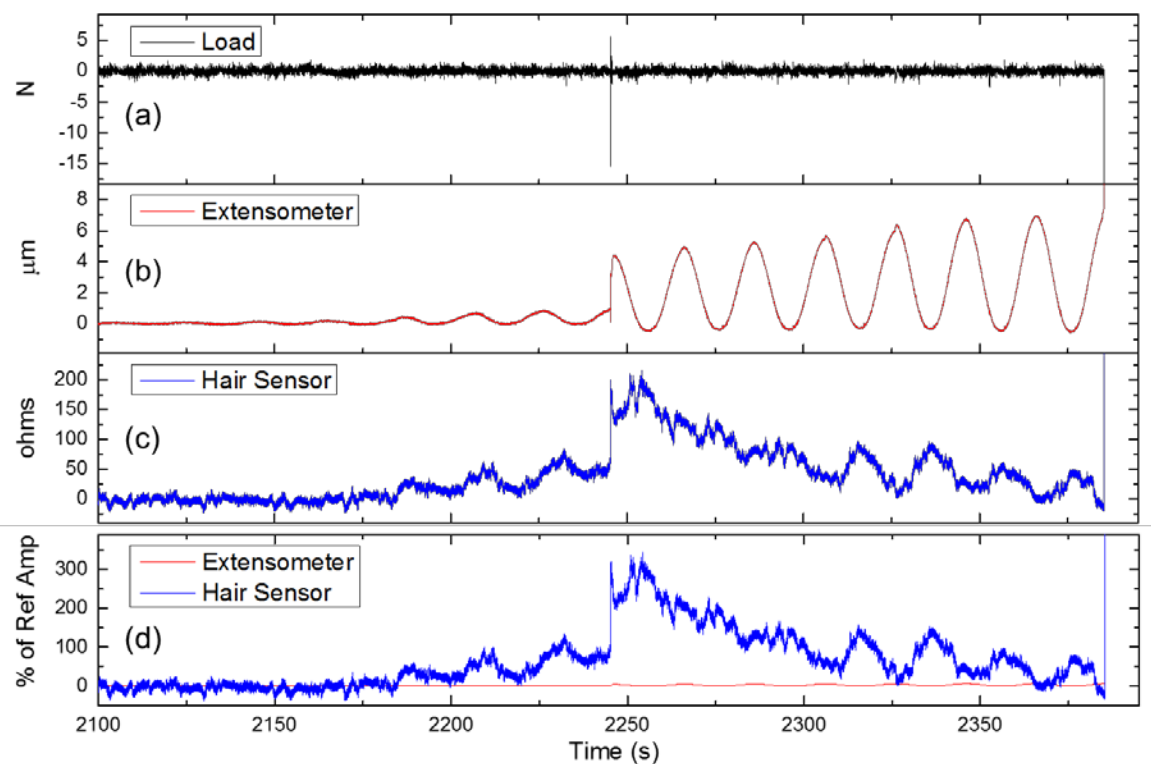
Figure 24. Response Deviation – Load Frame, Extensometer, and Hair Sensor

Note: Deviation in response near 2245 seconds referenced against the response over the previous 15 cycles of the (a) load frame, (b) extensometer, and (c) hair sensor. The anomaly at 2245 seconds is apparent in all three measurements and might be due to a partial disbond. (d) Comparison of percent of reference amplitude measurements from hair sensor and extensometer. The hair sensor displays a much greater response relative to its reference amplitude than does the extensometer.

3.5.4   Conclusions

A successful measurement of the relative displacement in a lap shear coupon was demonstrated for the first time, even though the resistance change was only about 0.1%. Conventional strain sensors cannot be used to measure out-of-plane motion such as shear. Other benefits of the embedded shear sensor include its footprint, which is much smaller than strain sensors and orders of magnitude smaller than the extensometer used here, as well as its ability to be embedded in a part. In these results, both the extensometer and the hair sensor indicated changes in the response of the sample prior to failure possibly demonstrating their ability to predict the onset of failure. In addition to being usable in the field were the extensometer cannot, the response of the sensor to the pre-failure changes of the sample was much more easily detectable with the hair sensor.

4.0   RESULTS AND DISCUSSION

A couple of sensors were successfully fabricated over the first few years of this effort. Now, sensors can be made and fully characterized at a rate of at least 1 per day, with on the order of 100 sensors having been successfully fabricated and "delivered" to various projects. Upcoming demonstrations with these devices could easily require hundreds of sensors per test article to perform airflow mapping and semiautonomous controls studies. A viable path for producing such quantities is needed.

The limits to the capabilities of individual sensors still need to be explored. For example, the following questions need to be investigated:

- Can the sensors distinguish between shapes of boundary layers?

- In the absence of knowledge of the boundary layer, what information can the sensors supply?

- One of the big advantages of hair sensors over pressure sensors is their ability to distinguish flow direction. Can the electrode of these sensors be easily patterned to enable this advantage in these devices?

The development of these devices has provided the opportunity to study the electromechanical properties of CNT arrays and evaluate their use for sensing applications. The sensors indeed provide a testbed for characterizing the stiffness and piezoresistivity of the CNT arrays. Unfortunately, however, the underlying source of these properties is not understood; likewise, the ability to finely control even the height of the nanotube arrays may prove impossible. In the absence of research that resolves these issues, sensors will have to be screened and sorted, which further increases the number of sensors required. Investigations into alternate transducing materials may also be worthwhile.

The environmental stability of the sensors has often been questioned, but remains to be studied. Methods for encapsulating the sensors or the nanotubes, if deemed necessary, have been suggested. Ideally, such investigations would also shed light on the nature of the long-term drift of the sensors.

The sensors have also be shown to be initially viable for detecting mechanical shear in bonded joints, a test that is impossible or prohibitively difficult with conventional sensors. This is especially true of sensors that can be fielded and embedded in structures. The ability of these sensors in this area needs to be further developed. The sensors could also be paired with conventional strain sensors to distinguish between tensile and flexural strain. Just as arrays of airflow sensors are being envisioned for spatial flow mapping, arrays of embedded structural sensors could provide spatial strain mapping across a structure.

The ability to embed and array sensors is limited by the ability to communicate information. Next generation multifunctional structures could include networks of signal structures ready to receive sensors and sensor packages without the need for back wiring.

Finally, better sensing of the environment and its impact on structure and flight will necessitate the need for structures that can adapt and respond to environmental impacts. Morphing and adaptive structures and materials need to be investigated and correlated to sensors for autonomous responses.

5.0 CONCLUSIONS

Here, the research team has demonstrated the fabrication, characterization, and performance of CNT-based artificial hair sensors as well as the synthesis of CNT arrays and methods for determining their electromechanical properties. The models used here to calculate the drag forces have been suggested elsewhere and are valid for small deflections of the hair. Differing from other sensors and measurements, these sensors are highly sensitive to small deflections, and the airflow inside the flow tube was well controlled and is well understood. The sensors were characterized and calibrated under controlled, benchtop conditions, such as with a point load, resulting in the ability to predict their response to airflow.

The nature of the compressive modulus and piezoresistivity in carbon nanotube arrays is still not yet able to be correlated to the properties of the individual nanotubes or predicted from the synthesis conditions. While difficult to measure by conventional methods, the compressive modulus of the radial nanotube arrays can be determined by fitting the displacement and curvature of the hair to that predicted by the model for a cantilever on a semi-infinite elastic base. The elastic base stiffness varied between devices by about an order of magnitude, but the normalized piezoresistivity was observed here to be about 0.6 across the devices and may be a more intrinsic property of CNT arrays.

In addition to demonstrating high sensitivity, the first-resonance bandwidth of the system was shown to perform well due to the large stiffness of the fiber relative to the mass of the hair including the CNTs and the large stiffness of the nanotube array relative to the stiffness hair. While the resonant frequencies can easily be approximated by treating the sensor as a cantilever fixed at the opening of the capillary, the resonant frequencies are also compatible with an elastic base model. This model indicated that the nanotubes are stiff enough to maximize the first-resonance bandwidth of the system, but it should also be possible to increase the sensitivity by decreasing the stiffness without significantly decreasing the bandwidth.

A model for nanotube growth within the capillary or similar high aspect ratio microcavities was presented. The taper of the nanotube profile – from long CNTs at near the openings to short in the middle – is a result of the competition between the diffusion of the reactants within the cavity and the kinetics of the reaction on the reactive surface.

The nominal and saturation resistances are partially a function of the electrical path down the shaft of the capillary through the nanotubes that are largely un-deformed even as the hair is deflected. The drift in these values might be due to temperature or humidity changes which could produce changes in CNT-CNT interconnectivity or thermal deformation. It is not known whether such drift is observed in planar arrays. Given the stability of these values for over 12 hours and the stability of the normalized response of over 2 weeks, the research team envisions re-characterizing the un-deflected and fully deflected resistance of the sensors at the beginning of each day of flights.

The team also demonstrated that the sensors can be used to detect the transition of flow from laminar to turbulent with a decrease in their average sensitivity to increasing air flow and a sharp increase in their otherwise constant RMS noise, indicating that the sensors are undergoing large vibration under turbulent flow. The flow over a wing can be laminar or turbulent, attached or separated, and wool tufts attached to the wing were used to visualize these flows. Likewise, it may be possible to use the sensors to detect and map these conditions electrically.

Finally, an alternative application for these sensors as mechanical shear sensors was investigated. When embedded within a lapshear joint, these sensors were able to detect the displacement due to a cyclic load similar to an extensometer. Differing from an extensometer, the footprint of the sensors is less than a millimeter, and they may be able to be fielded in a part rather than just a lab instrument. The sensors also displayed a larger relative change in response in advance of the failure of the sample.

The devices investigated here based on CNT arrays have been shown to be viable as low cost, high performance sensors for airflow or mechanical deformation sensing. They can either be operated as "insect grade" devices without much foreknowledge of their individual performance or – with straightforward calibration methods – as pseudo-instrument gauges able to give information about boundary layer characteristics and airspeed.

6.0   REFERENCES

1.   Humphrey, J.A.C.; Devarakonda, R.; Iglesias, I.; Barth, F.G. *Dynamics of arthropod filiform hairs. I. Mathematical modelling of the hair and air motions*. 1993; Vol. 340, p 423-444.
2.   Magal, C.; Dangles, O.; Caparroy, P.; Casas, J. Hair canopy of cricket sensory system tuned to predator signals. *Journal of Theoretical Biology* **2006**, *241*, 459-466.
3.   Camhi, J.M. Locust wind receptors: I. Transducer mechanics and sensory response. *Journal of Experimental Biology* **1969**, *50*, 335-348.
4.   Sterbing-D'Angelo, S.; Chadha, M.; Chiu, C.; Falk, B.; Xian, W.; Barcelo, J.; Zook, J.M.; Moss, C.F. Bat wing sensors support flight control. *Proceedings of the National Academy of Sciences* **2011**, *108*, 11291-11296.
5.   Brent, C.; Stephen, W.; Edward Haering, Jr.; Jerry, B.; Roback, V. Flush airdata sensing (fads) system calibration procedures and results for blunt forebodies. In *9th international space planes and hypersonic systems and technologies conference*, American Institute of Aeronautics and Astronautics: 1999.
6.   Dickinson, B.T.; Singler, J.R.; Batten, B.A. Mathematical modeling and simulation of biologically inspired hair receptor arrays in laminar unsteady flow separation. *Journal of Fluids and Structures* **2012**, *29*, 1-17.
7.   Shen, H.; Xu, Y.; Dickinson, B.T. Fault tolerant attitude control for small unmanned aircraft systems equipped with an airflow sensor array. *Bioinspiration & Biomimetics* **2014**, *9*, 046015.
8.   Junliang, T.; Xiong, Y. Hair flow sensors: From bio-inspiration to bio-mimicking—a review. *Smart Materials and Structures* **2012**, *21*, 113001.
9.   Maschmann, M.R.; Dickinson, B.; Ehlert, G.J.; Baur, J.W. Force sensitive carbon nanotube arrays for biologically inspired airflow sensing. *Smart Materials and Structures* **2012**, *21*, 094024.
10.   Ehlert, G.J.; Maschmann, M.R.; Baur, J.W. In *Electromechanical behavior of aligned carbon nanotube arrays for bio-inspired fluid flow sensors*, SPIE Active and Passive Smart Structures and Integrated Systems, 2011; pp 79771C-79771C-79715.
11.   SuhrJ; VictorP; CiL; SreekalaS; ZhangX; NalamasuO; Ajayan, P.M. Fatigue resistance of aligned carbon nanotube arrays under cyclic compression. *Nat Nano* **2007**, *2*, 417-421.
12.   McCrary-Dennis, M.C.; Okoli, O.I. A review of multiscale composite manufacturing and challenges. *Journal of Reinforced Plastics and Composites* **2012**, *31*, 1687-1711.
13.   Maschmann, M.R.; Ehlert, G.J.; Tawfick, S.; Hart, A.J.; Baur, J.W. Continuum analysis of carbon nanotube array buckling enabled by anisotropic elastic measurements and modeling. *Carbon* **2014**, *66*, 377-386.
14.   Maschmann, M.R.; Ehlert, G.J.; Park, S.J.; Mollenhauer, D.; Maruyama, B.; Hart, A.J.; Baur, J.W. Visualizing strain evolution and coordinated buckling within cnt arrays by in situ digital image correlation. *Advanced Functional Materials* **2012**, *22*, 4686-4695.
15.   Maschmann, M.R.; Zhang, Q.; Wheeler, R.; Du, F.; Dai, L.; Baur, J. In situ sem observation of column-like and foam-like cnt array nanoindentation. *ACS Applied Materials & Interfaces* **2011**, *3*, 648-653.
16.   Bedewy, M.; Farmer, B.; Hart, A.J. Synergetic chemical coupling controls the uniformity of carbon nanotube microstructure growth. *ACS Nano* **2014**, *8*, 5799-5812.

17. Amama, P.B.; Pint, C.L.; McJilton, L.; Kim, S.M.; Stach, E.A.; Murray, P.T.; Hauge, R.H.; Maruyama, B. Role of water in super growth of single-walled carbon nanotube carpets. *Nano Letters* **2008**, *9*, 44-49.

18. Puretzky, A.A.; Geohegan, D.B.; Jesse, S.; Ivanov, I.N.; Eres, G. In situ measurements and modeling of carbon nanotube array growth kinetics during chemical vapor deposition. *Appl. Phys. A* **2005**, *81*, 223-240.

19. Ehlert, G.; Maschmann, M.R.; Baur, J. In *Morphology control in hierarchical fibers for applications in hair flow sensors*, SAMPE, Long Beach, 2013; Long Beach.

20. Yamamoto, N.; John Hart, A.; Garcia, E.J.; Wicks, S.S.; Duong, H.M.; Slocum, A.H.; Wardle, B.L. High-yield growth and morphology control of aligned carbon nanotubes on ceramic fibers for multifunctional enhancement of structural composites. *Carbon* **2009**, *47*, 551-560.

21. Slinker, K.; Maschmann, M.R.; Kondash, C.; Severin, B.; Phillips, D.; Dickinson, B.T.; Reich, G.; Baur, J. In *Variable deflection response of sensitive cnt-on-fiber artificial hair sensors from cnt synthesis in high aspect ratio microcavities*, SPIE Smart Structures/NDE, 2015; pp 942917-942917-942913.

22. Yamamoto, N.; Guzman de Villoria, R.; Wardle, B.L. Electrical and thermal property enhancement of fiber-reinforced polymer laminate composites through controlled implementation of multi-walled carbon nanotubes. *Composites Science and Technology* **2012**, *72*, 2009-2015.

23. Wicks, S.S.; Wang, W.; Williams, M.R.; Wardle, B.L. Multi-scale interlaminar fracture mechanisms in woven composite laminates reinforced with aligned carbon nanotubes. *Composites Science and Technology* **2014**, *100*, 128-135.

24. Wicks, S.S.; de Villoria, R.G.; Wardle, B.L. Interlaminar and intralaminar reinforcement of composite laminates with aligned carbon nanotubes. *Composites Science and Technology* **2010**, *70*, 20-28.

25. Sager, R.J.; Klein, P.J.; Lagoudas, D.C.; Zhang, Q.; Liu, J.; Dai, L.; Baur, J.W. Effect of carbon nanotubes on the interfacial shear strength of t650 carbon fiber in an epoxy matrix. *Composites Science and Technology* **2009**, *69*, 898-904.

26. Zhang, F.-H.; Wang, R.-G.; He, X.-D.; Wang, C.; Ren, L.-N. Interfacial shearing strength and reinforcing mechanisms of an epoxy composite reinforced using a carbon nanotube/carbon fiber hybrid. *J Mater Sci* **2009**, *44*, 3574-3577.

27. Qian, H.; Bismarck, A.; Greenhalgh, E.S.; Shaffer, M.S.P. Carbon nanotube grafted carbon fibres: A study of wetting and fibre fragmentation. *Composites Part A: Applied Science and Manufacturing* **2010**, *41*, 1107-1114.

28. Ren, X.; Burton, J.; Seidel, G.D.; Lafdi, K. Computational multiscale modeling and characterization of piezoresistivity in fuzzy fiber reinforced polymer composites. *International Journal of Solids and Structures* **2015**, *54*, 121-134.

29. Sebastian, J.; Schehl, N.; Bouchard, M.; Boehle, M.; Li, L.; Lagounov, A.; Lafdi, K. Health monitoring of structural composites with embedded carbon nanotube coated glass fiber sensors. *Carbon* **2014**, *66*, 191-200.

30. Maschmann, M.R.; Zhang, Q.; Du, F.; Dai, L.; Baur, J. Length dependent foam-like mechanical response of axially indented vertically oriented carbon nanotube arrays. *Carbon* **2011**, *49*, 386-397.

31. Deck, C.P.; Flowers, J.; McKee, G.S.B.; Vecchio, K. Mechanical behavior of ultralong multiwalled carbon nanotube mats. *Journal of Applied Physics* **2007**, *101*, 23512-23511.

32. Cao, A.; Dickrell, P.L.; Sawyer, W.G.; Ghasemi-Nejhad, M.N.; Ajayan, P.M. Super-compressible foamlike carbon nanotube films. *Science* **2005**, *310*, 1307-1310.

33. Poenitzsch, V.; Slinker, K.; Miles, D.; Miller, M.; Wei, R.; Coulter, K.; Gardner, S. Freestanding foils of nanotube arrays fused with metals. *J Mater Sci* **2014**, *49*, 7080-7086.

34. Phillips, D.M.; Slinker, K.A.; Ray, C.W.; Hagen, B.J.; Baur, J.W.; Dickinson, B.T.; Reich, G.W. Artificial hair sensors: Electro-mechanical characterization. **2014**, V002T006A016.

35. Maschmann, M.R.; Ehlert, G.J.; Dickinson, B.T.; Phillips, D.M.; Ray, C.W.; Reich, G.W.; Baur, J.W. Bioinspired carbon nanotube fuzzy fiber hair sensor for air-flow detection. *Advanced Materials* **2014**, *26*, 3230-3234.

36. Gao, Y.; Kodama, T.; Won, Y.; Dogbe, S.; Pan, L.; Goodson, K.E. Impact of nanotube density and alignment on the elastic modulus near the top and base surfaces of aligned multi-walled carbon nanotube films. *Carbon* **2012**, *50*, 3789-3798.

37. Boresi, A.P.; Schmidt, R.J. *Advanced mechanics of materials*. 6th ed.; John Wiley & Sons: New York, 2003; p xiii, 681 p.

38. Andrews, R.; Jacques, D.; Rao, A.M.; Derbyshire, F.; Qian, D.; Fan, X.; Dickey, E.C.; Chen, J. Continuous production of aligned carbon nanotubes: A step closer to commercial realization. *Chemical Physics Letters* **1999**, *303*, 467-474.

39. Li, X.; Ci, L.; Kar, S.; Soldano, C.; Kilpatrick, S.J.; Ajayan, P.M. Densified aligned carbon nanotube films via vapor phase infiltration of carbon. *Carbon* **2007**, *45*, 847-851.

40. Futaba, D.N.; Hata, K.; Namai, T.; Yamada, T.; Mizuno, K.; Hayamizu, Y.; Yumura, M.; Iijima, S. 84% catalyst activity of water-assisted growth of single walled carbon nanotube forest characterization by a statistical and macroscopic approach. *The Journal of Physical Chemistry B* **2006**, *110*, 8035-8038.

41. Endo, H.; Kuwana, K.; Saito, K.; Qian, D.; Andrews, R.; Grulke, E.A. Cfd prediction of carbon nanotube production rate in a cvd reactor. *Chemical Physics Letters* **2004**, *387*, 307-311.

42. Stefan, J. Uber einige probleme der theorie der warmeleitung. *S.-B. Wien-Akad. Mat. Natur.* **1889**, *98*, 173-184.

43. Carty, R.; Schrodt, T. Concentration profiles in ternary gaseous diffusion. *Industrial & Engineering Chemistry Fundamentals* **1975**, *14*, 276-278.

44. White, F.M. *Viscous fluid flow*. McGraw-Hill: New York,, 1974; p xix, 725 p.

45. Chen, J.; Fan, Z.; Zou, J.; Engel, J.; Liu, C. Two-dimensional micromachined flow sensor array for fluid mechanics studies. *Journal of Aerospace Engineering* **2003**, *16*, 85-97.

46. Krijnen, G.; Floris, A.; Dijkstra, M.; Lammerink, T.; Wiegerink, R. In *Biomimetic micromechanical adaptive flow-sensor arrays*, 2007; pp 65920F-65920F-65915.

47. Casas, J.; Dangles, O. Physical ecology of fluid flow sensing in arthropods. *Annual Review of Entomology* **2010**, *55*, 505-520.

48. Nannan, C.; Tucker, C.; Engel, J.M.; Yingchen, Y.; Saunvit, P.; Chang, L. Design and characterization of artificial haircell sensor for flow sensing with ultrahigh velocity and angular sensitivity. *Microelectromechanical Systems, Journal of* **2007**, *16*, 999-1014.

49. Sarlo, R.; Leo, D.; Tarazaga, P. Spectral analysis and characterization of a membrane-based artificial hair cell sensor. **2014**, V002T006A010.

50. Chandrasekaran, V.; Cain, A.; Nishida, T.; Cattafesta, L.N.; Sheplak, M. Dynamic calibration technique for thermal shear-stress sensors with mean flow. *Exp Fluids* **2005**, *39*, 56-65.

51. Shimozawa, T.; Kumagai, T.; Baba, Y. Structural scaling and functional design of the cercal wind-receptor hairs of cricket. *J Comp Physiol A* **1998**, *183*, 171-186.

52. Eisenberger, M.; Yankelevsky, D.Z.; Adin, M.A. Vibrations of beams fully or partially supported on elastic foundations. *Earthquake Engineering & Structural Dynamics* **1985**, *13*, 651-660.

APPENDIX A

**Procedures for AHS Fabrication
(as Performed in AFRL/RXCC Laboratories)**

Procedure for Cutting and Polishing Capillaries

1. Capillaries should be bunched together inside a glass tube infused with resin (Epon 828 – Jeffamine D230) to hold in place.
   a. Cure this in oven
2. Cut sections of this stock to 1.8-2mm length with diamond saw.
3. Fix these sections on a metal polishing platen with crystal bond by heating.
4. Grind down with 600 grit paper to ~ 1.7mm length. Run water during grind.
   a. 110 RPM with force of 1lb for 1.5 minutes
5. Grind down with 800 grit paper to ~ 1.6mm length. Run water during grind.
   a. 110 RPM with force of 1lb for 1.5 minutes
6. Use fine polishing pad while spraying alumina particles suspended in water for final polish until a mirror like finish.
   a. Check surface roughness with optical microscope.
7. Flip capillaries over on platen to grind and polish other face.
8. Grind down with 600 grit paper to ~ 1.5mm length. Run water during grind.
   a. 110 RPM with force of 1lb for 1.5 minutes
9. Grind down with 800 grit paper to ~ 1.2 - 1.3mm length. Run water during grind.
   a. 110 RPM with force of 1lb for 1.5 minutes
10. Use fine polishing pad while spraying alumina particles suspended in water for final polish until a mirror like finish.
    a. Check surface roughness with optical microscope.
11. Heat the platen to remove capillaries.
12. Clean platens with acetone
13. Soak the pieces in acetone overnight to remove resin.
14. Rinse capillaries with acetone next day.
15. Clean with ethanol.
16. Put capillaries in a high temp ceramic boat.
17. Burn off capillary skin in oven at 700°C for 10 min.
18. Let caps come to room temp.
19. Sonicate in ethanol for 15 minutes.

Procedure for Depositing Electrodes

For use with Denton Vacuum Sputtercoater:

1. Open Argon gas cylinder valve & regulator valve
   a. Do NOT adjust middle knob on gas cylinder setup
2. Open vacuum menu on digital display, Turn off Turbo pump
   a. Wait 5-10minutes or until turbo @ speed" message goes away
3. Turn off Rough pump
4. Lift cover lid using post. Do NOT lift by pulling up on the chamber lid
5. Load sample into chamber, handling with gloves, replace lid
6. Turn on Rough pump
   a. Wait until digital display reads <100mtorr on system screen
7. Turn on Turbo pump
   a. Wait until system reaches ~10^{-6} torr on standalone gauge
8. Open gas valve using digital display
   a. Adjust pressure to 5×10^{-3} torr using gas control knob
9. Open Timed Sputter menu on digital display
   a. Set Sputter Settpoint to 30%
   b. Set duration to appropriate amount (600 seconds)
10. Start
    a. A slight purple glow should be visible thru the portal, indicative of plasma
    b. Increase Sputter Power by 1-2% until Current reaches target of 39mA
       i. Typically correlates to a Sputter Power of ~38%
11. Once time has elapsed, turn off Turbo pump
    a. Wait 5-10minutes or until "turbo @ speed" message goes away
    b. Or expose low pressure of Argon gas using gas control knob
12. Turn off Rough pump
13. Close Argon gas cylinder
14. Lift cover lid using post. Do NOT lift by pulling up on the chamber lid
15. Remove sample, handling with gloves, replace lid
16. Turn on Rough pump
    a. Wait until system pressure <100mtorr
17. Turn on Turbo pump

*System should be left under vacuum with both Turbo & Rough pumps activated

Procedure for Depositing Alumina on Fibers by ALD

-Coating glass hair fibers, silicon wafers w/ thermal oxide layer, glass slides w/ Kapton tape

1. ALD system is first come first serve.
    a. Sign in the book if you will be using it.
    b. Note the number of cycles you will be running (note operating temp adjacent)
        i. Typically 100 cycles @ 200C
    c. Note the gauge pressure from the labview window
        i. If gauge pressure is 10E^(-7) torr then the pressure gauge is likely loose
            1. Tighten the cord (looks like Ethernet underneath top right)
2. The nitrogen should be kept closed when not in operation
    a. When ready to use, open nitrogen valve (small, black knob, facing down)
3. Remove the heat shield
4. Open the Savannah ALD labview driver software
    a. If the software is not open, good chance the system has come to room temp.
    b. Will need to give a few hours for system to come to temp before use
5. Check underneath that the trimethylaluminum valve is open. (flat sides should be in line/parallel with tube)
6. Load the program recipe
    a. Right click in cells
    b. Click load recipe
    c. Choose alumina 200
    d. Line 16 – goto – 12 – 100 (this final number is number of cycles)
7. Check that the manifold is at 150C
8. Both top and bottom heat plates will come to 200C when program starts
9. Click vent
10. Open the lid and load sample
    a. Deposition only works well in center along line of gas flow
    b. Don't put samples above or below the line
    c. Use something to hold samples down (glass slides)
11. Close lid and hold down handle lightly when clicking pump
12. Wait until the pressure flattens out then click start (MOVE MOUSE AWAY FROM BUTTONS)
13. 100 cycles (~10nm) takes approx. 28 mins
14. When done click vent
15. Unload samples
16. CLOSE THE NITROGEN KNOB AT END OF RUN

KEEP SYSTEM PUMPING AT END OF DAY

Procedure for Synthesizing Carbon Nanotube Arrays

-Argon & Hydrogen mass flow controllers, o-Xylene & Ferrocene chemicals

17. Check that furnace is at room temp.
18. If the tube has lots of carbon in it:
    a. Take temp up to 900C to burn it all out (leave the ends open).
19. If tube looks pretty good (only red iron residue):
    a. Get texwipe, ethanol, and brush (clean out quartz tube ~3 times).
20. Putting together tube:
    a. Teflon washer insert on outer side of both sides. (4 total)
        i.   2 way adapters on both sides.
        ii. Keep them facing same direction on both sides.
        iii. Stand up the tube on both feet of these adapters.
        iv. Hand tighten the brass fittings.
        v.   Use the tightening tool to secure outermost pieces.
    b. Hand vacuum (vacuum parts drawer).
        i.   Press down on black 2 way button and pump until 25 in-Hg.
        ii. Put on gas line, KF flange be careful not to move/twist tube!
21. MKS power supply (Make sure all are closed)
    a. Set point, flow is the reading you actually get. (Make sure all are closed)
22. Use rod with hook on it to clean out the injection tube.
    a. Insert from syringe side so not to torque injection side.
    b. Wash with acetone then ethanol into beaker with kimwipe in it.
    c. Use nitrogen hose to blow out tube.
23. Prepare Xylene and Ferrocene solution.
    a. 30 mL beaker, weigh paper, pipet, syringe, texwipes, parafilm, scoopula.
    b. Weigh 5% Ferrocene by weight in Xylene.
        i.   5g Xylene (Under Snorkel).
        ii. 0.25g Ferrocene.
    c. Combine chemicals in beaker and put Parafilm over.
    d. Sonicate for 20 seconds.
    e. Fill up syringe and push out air bubble (be very careful).
    f. Put syringe in syringe pump holder.
        i.   Use slot just behind the middle swivel. (make sure there is a syringe on other side)
24. Prep samples on graphite slide (sensors & glass fibers with silica over them).
    a. Sensor orientation is perpendicular to opening of tube.
25. Insert samples into tube using external glass tubing.
    a. Want silver line on injection side of quartz tube to line up with inner edge of recessed furnace valley.
    b. Want center of graphite slide to be in center of thermocouple in middle of furnace.

26. Furnace should be at room temp.
    a. Hold down Set/Ent. Leave it in mode res, hit enter
    b. Hit enter, get to program menu (up/down) to program 1
    c. We change prgm 1
    d. Hit enter
    e. SSP – 25, enter
    f. Stc – 0, enter
    g. Sp1 – 750, enter
    h. Em1 – 0.20, (20 mins to get to 750) enter
    i. Sp2 – 750, (hold temp) enter
    j. En2 – 1.25, (hold time @ 750) enter
    k. Sp3 – 25, (back to room temp) enter
    l. En3 – off, (turn off furnace) enter
    m. Hold down set/ent until it gets to main screen
27. Make sure O-rings with metal inserts are on either end of tube.
    a. Put on the KF flanges and hand tighten.
28. Check calibration sheets; match SSCM (Standard Cubic Centimeters per Minute) with set point.
    a. We want 500sccm Argon – Set point 660sccm (MKS controller).
    b. We want 50sccm Hydrogen – Set point 120sccm (MKS controller).
29. Turn on Argon & Hydrogen – check flow reading of each individually, check for bubbling.
30. Syringe pump program:
    a. Get dispensed light on by pushing volume button.
    b. Hold rightmost up arrow to reset display.
    c. Get dispensed light off to set volume.
31. Priming injection tube:
    a. Set volume to 0.8mL
    b. Set rate to 1.0
    c. Set units to mL/min
    d. Make sure withdraw light is not on (means ready to pump)
32. Set timer for less than 20 minutes (start it when you turn on furnace)
    a. Hold down run until furnace turns on, it will come to temp
    b. Make sure Argon and Hydrogen gases are flowing.
33. Clean up equipment used and trash!
34. When furnace gets to 750C (it will overshoot a few degrees, wait to come back to 750):
    a. Hit pump on syringe pump. (it will inject 0.8mL @ 1mL/min)
    b. Once it reaches 0.8mL:
    c. Hold the rightmost up arrow to reset display
    d. Set volume to 0.4mL
    e. Rate already set at 1.0

f. Set units to mL/hr
g. Hit start
35. It will inject 0.4mL @ 1mL/hr = 24minutes (0.4*60min= 24min run time)
a. Set timer for less than 24 minutes
36. When volume reaches 0.4mL:
a. Hit left/right arrows button to get withdraw light on
b. Hold start button
c. It will withdraw fluid until small bubble comes into syringe
d. Hold down reset button and the furnace will shut off and cool down
e. Turn off hydrogen gas
37. Wait ~20min for furnace to cool down below 500C.
a. Crack open with the brick and place the fan to cool tube
b. Wait until down at 200C to open furnace all the way
i. Take off right flange
38. Take out samples @ 200C
39. Get texwipe, ethanol, and brush (clean out quartz tube ~3 times).
40. Return to step 8 to run more growths.
41. At end of day:
a. Turn off Argon gas on MKS controller (both gases should now be off)
b. Dispose leftover Xylene/Ferrocene solution in container by sink marked: (Recovered)
c. Use rod with hook on it to clean out the injection tube.
i. Insert from syringe side so not to torque injection side.
ii. Wash with acetone then ethanol into beaker with kimwipe in it.
iii. Use nitrogen hose to blow out tube.

# Procedure for Testing Sensors with the Benchtop Point Deflection Setup

1. Lock fixture by tightening set screw on front using hex wrench.
2. Unload sensor by unscrewing set screws on the right side of fixture. Use Carbon tweezers to lift sensor out and place it back in its proper container.
   a. Be sure the orientation of the sensor is correct with top/bottom in correct direction.
3. Put new sensor in place noting orientation of the hairs.
4. Push side fixture against side of sensor to make good contact with front/back electrode
5. To assure good contact between electrodes, check contact resistances of the sensor to the fixture. Use FLUKE voltmeter to measure contact resistances.
6. Lock down sensor by tightening set screws on right side of fixture.
   a. Check front contact - Plug in Black and Green.
   b. Check rear contact – Plug in Red and White.
   c. If showing no resistance – means open circuit – adjust fixture so contact can be made.
   d. If resistances are high (Mohms) – means bad contact. Adjust so resistances are in kohm-ohm range.
      i. If only 1 of 4 electrodes is in Mohms that's ok.
7. Once contact resistances are good, measure resistances through the device.
   a. Plug in Black and Red. Note resistance.
   b. Plug in Black and White. Note resistance.
   c. Plug in Green and White. Note resistance.
   d. Plug in Green and Red. Note resistance.
8. Pair with highest resistance goes into sense-4wire on Keithley.
9. Pair with lowest resistance goes into input/output on Keithley.
10. Click (ohm symbol) on Keithley.
11. Click On button to read resistance. Make sure it is same as before.
12. Open Conex GUI.
13. Actuator will be at previous position.
14. Make sure stage is LOCKED
15. Hit initialize.
16. Adjust actuator until it is close to stage arm. So that hair will not be chopped off.
17. Unlock stage
18. Use GUI to move stage until optically "just in contact" with the hair.
19. Find both start positions for left and right blade. Save position and the rename position.
20. Open LabVIEW. Open R vs T.
21. VISA resource name. Select GPIB########.
22. Millisecond/interval = 100
23. Check both 4pt measurement or 2pt measurement.
   a. Choose 4pt unless 2pt is a lot better with noise.
24. Go back to CONEX GUI
25. Use 0.4mm velocity for general movements.
   a. Use 0.005mm per second velocity for measurements
26. Start with 0.1mm total deflection.

a. Paste start position into absolute position. Add the 0.1mm to that and put
   i. Moving hair to the right 'Left Blade' (15.6-15.7) (100micron change)
   ii. Moving hair to the left 'Right Blade' (12.0-11.9) (100micron change)
27. Hit the start button on LabVIEW window to start taking data
    a. Note start time in LabVIEW filename
28. Save files as .txt

Once we have determined what the maximum deflection should be in each direction.

Cycles

1. Run 5 cycles in each direction
2. Run Left Blade Test 1ce then Right Blade Test 1ce then Left Blade Test 1ce.
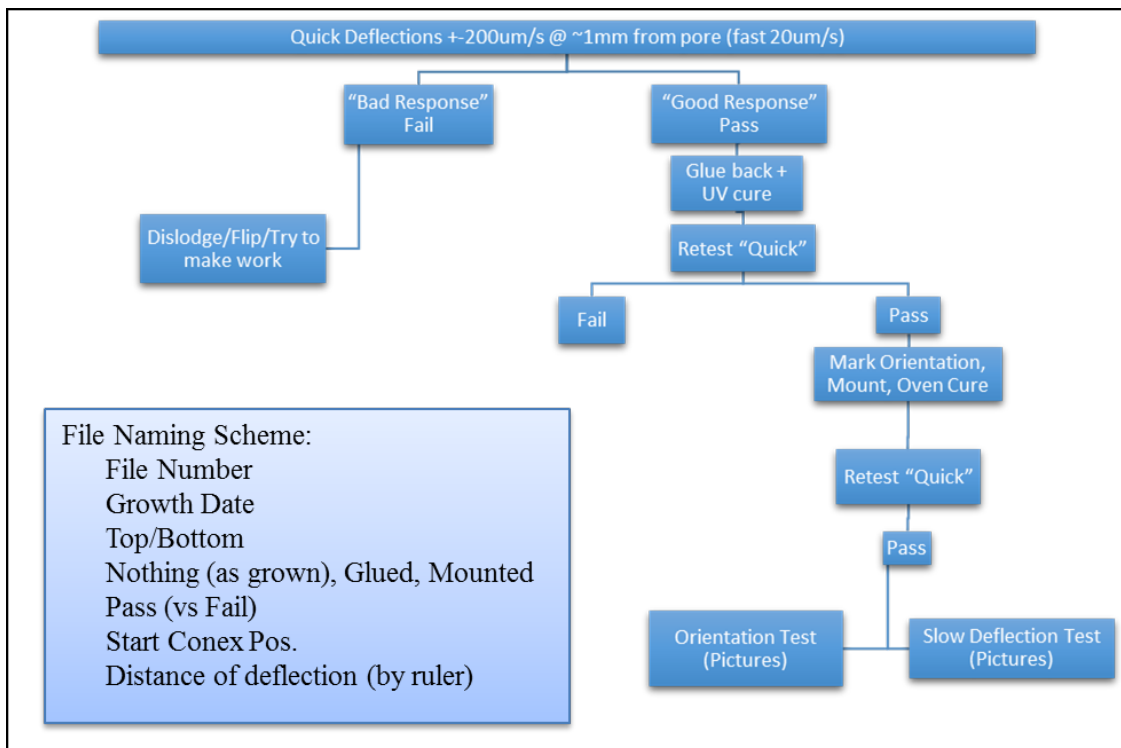
Figure A-1. Flow Chart for Screening, Tuning, and Collecting Baseline Deflection Response

Note: (inset) File naming scheme.

Procedure for Measuring the Hair Length and CNT Array Length

Procedure for Measuring the Exposed Hair Length (L_E), CNT Array Length (L_{CNT}), and Surface Area of Hair

1. Use 2.5x objective, auto exposure, medium contrast.
    a. These measurements are done in the clear Ted Pella sample cases with the glass board on the microscope stage.
2. Line up the hair so that it is straight from left to right on the screen. (capillary on left, hair sticking out to the right)
3. Zoom in on the capillary opening with the click wheel on the mouse.
4. Right click on the spot where the hair just starts coming out of the capillary opening (sometimes you need to click a little further from the pore opening because there might still be dark spots above and below the hair that might screw with the image contrast recognition.)
5. Click "Move this point to center"
6. Over in the XY stage control panel, set the stage movement to half of the screen width (~2435 µm) and click move stage to the right so that the capillary is now off the screen and only the hair is shown coming out from the left side of the screen.
7. Zoom in right where the hair is sticking out from the left side of the screen and fine focus so that the hair appears darkest.
8. In DS-fi1 settings, set the capture quality to 2560X1920
9. Click capture image
10. Zoom out so that you can see the whole hair
11. Measure the length of the hair and record this in an excel sheet or notebook.
12. In menu click Binary > Define Threshold > Per Channel > Drag the sliders on the histogram until only the hair is highlighted in blue on the image > click OK > In the Area portion of the measurements and annotations settings click on "Select Binary" > click on the blue highlighted hair > as long as it looks like it only selecting the hair record the area measurement in excel.
13. SAVE THE IMAGE!
    a. (This does not save the measurements you made on the screen – only the image itself).

**To measure the CNT Array Length, zoom close to the base of the hair near the pore opening, measure the diameter of the total hair, subtract the diameter of the glass fiber and divide by 2 to get L_{CNT}.

APPENDIX B

Preliminary Investigation of Aligned Carbon Nanotubes as Resistive Heaters for Out-of-Autoclave Curing of Composites

Project Summary

Within the scope of this task order, UTC subcontracted a small seed study to the Massachusetts Institute of Technology (MIT), under the leadership of Prof. Brian Wardle, to provide a preliminary investigation of aligned carbon nanotube (A-CNT) network heaters to assist the manufacture of laminated aerospace composite materials. Prof. Wardle's team successfully extended the understanding of the basic physics, as well as demonstrated this new application, of utilizing A-CNT network heaters for this purpose. Prior work had demonstrated the concept with autoclave prepreg, while this study extended the work to an out-of-autoclave material of interest to AFRL, namely Cytec 5320-1.

The funding partially supported the characterization and physical mechanism work documented in a joint paper published in *Applied Physics Letters* (vol. 106), as well as partially supported the demonstration of "out of oven" curing reported in *ACS Applied Materials & Interfaces* (vol. 7). One particular investigation suggested by AFRL/RXCC collaborators was to explore limits of the heaters in air. The second paper reports this work, in which the MIT team showed that the heaters were stable for approximately 1 hour (the length tested) in air at 550°C. These results suggest that a wide range of aerospace structural polymers may be fabricated using this approach, such as PMR-15 as well as polyether ether ketone (PEEK) and polyetherketoneketone (PEKK) thermoplastics. The MIT project support enabled UTC and AFRL/RXCC to evaluate the potential of resistive heating by A-CNT networks for further study.

Further Information:

1. Lee J.; Stein I.Y.; et al. Impact of carbon nanotube length on electron transport in aligned carbon nanotube networks, *Applied Physics Letters*, **2015**, *106*, 053110.
2. Lee J.; Stein I.Y.; Kessler S.S.; Wardle B. Aligned carbon nanotube film enables thermally induced state transformations in layered polymeric materials, *ACS Applied Materials & Interfaces*, **2015**, *7 (16)*, 8900-8905.

List of Symbols, Abbreviations, and Acronyms

ACRONYM	DEFINITION
A-CNT	Aligned Carbon Nanotube
ACS	American Chemical Society
ADS	Air Data Systems
AFRL	Air Force Research Laboratory
AHS	Artificial Hair Sensor
AoA	Angle of Attack
AoS	Angle of Sideslip
CNT	Carbon Nanotube
DOD	Department of Defense
DTIC	Defense Technical Information Center
EAR	Export Administration Regulation
FIB	Focused Ion Beam
ITAR	International Traffic in Arms Regulation
M&P	Materials & Processes
MEMS	Microelectromechanical Systems
MIT	Massachusetts Institute of Technology
OMC	Organic Matrix Composites
R&D	Research and Development
RX	Materials & Manufacturing Directorate
RXC	Structural Materials Division
RXCC	Composites Branch
SEM	Scanning Electron Microscope
TOPS IV	Technical Operations IV
USAF	United States Air Force
UTC	Universal Technology Corporation
WPAFB	Wright-Patterson Air Force Base